Chapter 6
Methane Monooxygenase: Functionalizing Methane at Iron and Copper

Matthew H. Sazinsky and Stephen J. Lippard

Contents

M.H. Sazinsky
Department of Chemistry, Pomona College, Claremont, CA 91711, USA
e-mail: matthew.sazinsky@pomona.edu

S.J. Lippard (✉)
Department of Chemistry, Massachusetts Institute of Technology,
Cambridge, MA 02139, USA
e-mail: lippard@mit.edu

Abstract Methane monooxygenases (MMOs) catalyze the conversion of methane to methanol as the first committed step in the assimilation of this hydrocarbon into biomass and energy by methanotrophs, thus playing a significant role in the biogeochemistry of this potent greenhouse gas. Two distinct enzymes, a copper-dependent membrane protein, particulate methane monooxygenase (pMMO), and an iron-dependent cytosolic protein, soluble methane monooxygenase (sMMO), carry out this transformation using large protein scaffolds that help to facilitate the timely transport of hydrocarbon, O_2, proton, and electron substrates to buried dimetallic active sites. For both enzymes, reaction of the reduced metal centers with O_2 leads to intermediates that activate the relatively inert C–H bonds of hydrocarbons to yield oxidized products. Among synthetic and biological catalysts, MMOs are unique because they are the only ones known to hydroxylate methane at ambient temperatures. As a need for new industrial catalysts and green chemical transformations increases, understanding how the different MMO metal centers efficiently accomplish this challenging chemistry has become the focus of intense study. This chapter examines current understanding of the sMMO and pMMO protein structures, their methods for substrate channeling, and mechanisms for the dimetallic activation of O_2 and C–H bonds.

1 Introduction

Methanogens living in anaerobic environments produce greater than 200–250 million metric tons of methane per year as a byproduct of catabolizing biomass [1]. Taking advantage of this unique waste product, methanotrophs evolved to survive at the interface between anaerobic and aerobic worlds where they require both methane and O_2 for the metabolic assimilation into macromolecules and stored energy [2]. By using methane as a primary carbon and energy source, methanotrophs limit the escape of this potent greenhouse gas into the atmosphere and thereby lessen its global environmental impact [2, 3]. Responsible for catalyzing the conversion of methane to methanol and initiating biomass assimilation in methanotrophs are methane monooxygenases (MMOs), of which two distinct forms exist. The most prevalent, and least understood, form is the copper-utilizing membrane-bound or particulate MMO (pMMO), which can account for up to 20 % of the total protein in methanotrophs [4–7]. The iron-containing cytosolic or soluble MMO (sMMO), found only in some methanotrophic species, is better characterized [8–11]. Both enzymes have received significant attention because they routinely carry out one of the most difficult chemistries in nature, the breaking of a relatively inert and high energy C−H bond (104 kcal/mol) at ambient temperatures. Other iron, copper, and cytochrome P450 monooxygenases that readily hydroxylate larger, more reactive hydrocarbons cannot oxidize methane, making MMOs unique catalysts.

Isolated from a variety of different environments, most acidophilic, alkaliphilic, psychrophilic, thermophilic, and mesophilic methanotrophs except for the *Methyocella* genus contain genes for pMMO, suggesting that it is the predominate MMO in the environment [2, 12]. Some species, which include extensively studied *Methylococcus capsulatus* (Bath) and *Methylosinus trichosporium* OB3b, differentially express both pMMO and sMMO based on copper availability [13–16]. High environmental copper suppresses sMMO translation in these organisms and induces the expression of pMMO as well as the synthesis of intracytoplasmic membranes into which pMMO is incorporated. Conversely, low copper concentrations lead to sMMO expression and synthesis of methanobactins, copper scavenging compounds or chalkophores, with properties and functions like those of the widely studied siderophores [17–20].

Structurally and mechanistically, there are few similarities between pMMO and sMMO. However, both of these enzymes share one important task, the efficient generation of oxidized hydrocarbon products by coordinating the reactivity of four

substrates (hydrocarbon, oxygen, electrons, and protons) at a highly reactive dimetallic center. Methane is the primary MMO substrate that can most readily be funneled into lower metabolic pathways for the purposes of carbon assimilation and energy production via the serine and ribulose monophosphate pathways (Figure 1) [2].
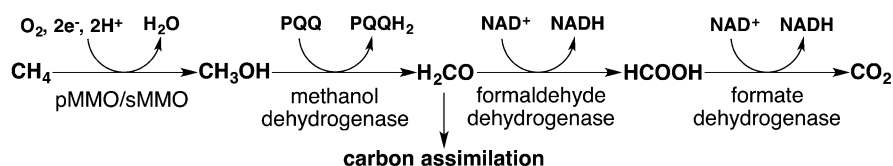

Figure 1 Metabolic pathway for hydrocarbon assimilation in methanotrophs.

pMMO and sMMO, however, are capable of regio- and stereospecifically hydroxylating a wide variety of hydrocarbon substrates. Whereas sMMO can act on linear and branched alkanes and alkenes of up to eight carbons in length, in addition to aromatic, heterocyclic, and halogenated compounds [21–26], pMMO is more selective toward alternative substrates with preferences for alkanes and alkenes of up to five and four carbons, respectively [3, 27–29]. Because they are such powerful catalysts, the iron and copper centers of sMMO and pMMO, respectively, have been investigated intensely for their potential wide-ranging applications to synthesis and environmental remediation [3, 22]. This chapter focuses on the current knowledge of the pMMO and sMMO systems and how they carry out their respective enzymatic functions.

2 Particulate Methane Monooxygenase

pMMO comprises three polypeptide chains, a 45-kDa α-subunit (pmoB), a 26-kDa β-subunit (pmoA), and a 23-kDa γ-subunit (pmoC), that assemble into a homotrimer with an $(\alpha\beta\gamma)_3$ configuration (Figure 2 and Figure 3 below) [30]. Because pMMO is vital to the survival of most methanotrophs, several species contain duplicate copies of the *pmoCAB* genes [31]. The closely related pMMO homolog, ammonia monooxygenase (AMO), is the only other known enzyme that can oxidize methane, and its composition is similar to that of pMMO [32]. Over the years, different approaches by several laboratories toward the purification and biochemical and spectroscopic characterization of pMMO have generated much debate and confusion in the literature about the metal content, metal type, subunit stoichiometry, and active site location. For example, purifications of pMMO from *M. capsulatus* (Bath) and *M. trichosporium* OB3b have generated results suggesting that it contains 2, 2–3, 8–10, and 15–20 coppers per αβγ protomer as well as significant quantities of iron, ~0.75–2.5 ions/protomer [14, 33–39].
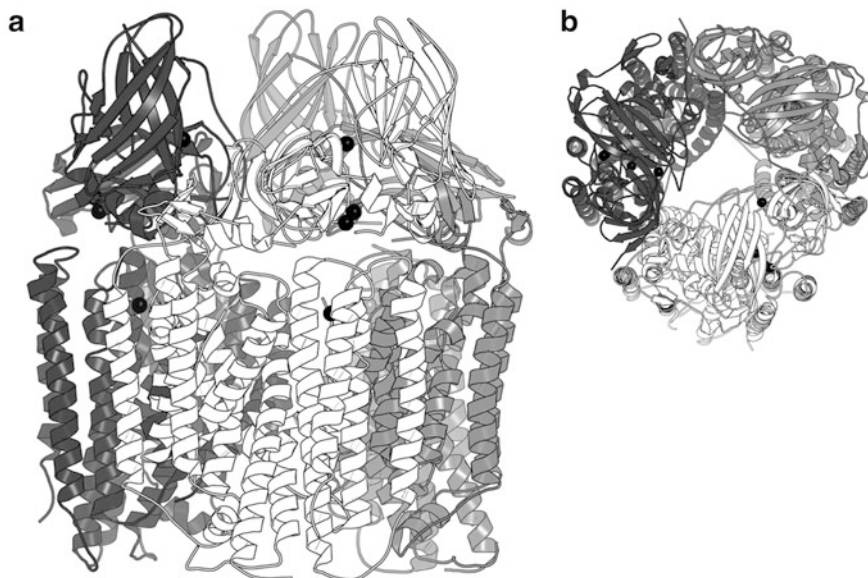
Figure 2 (**a**) Global structure of pMMO (PDB entry 3RGB) depicting each of the three αβγ protomers. (**b**) Top down view of the cytosolic pMMO pmoB cupredoxin-like domains depicting the channel through the protein. The metal centers are shown as black spheres.

From spectroscopic investigations, mononuclear, dinuclear, and trinuclear copper sites, as well as a diiron center, have all been proposed for the pMMO active site [5, 12, 40]. The inherent complexities with working on a membrane protein coupled with the difficulty of identifying the nature of the pMMO active site explain why our understanding of pMMO has lagged behind that of sMMO. Fortunately, significant strides have been made recently that bring clarity to the problem and a better understanding of pMMO. The following sections are not intended to be an exhaustive treatment of the pMMO literature, but instead aim to present the most reasonable and clear picture to date as to how this protein operates.

2.1   Architecture

The first crystal structure of pMMO from *Methylococcus capsulatus* (Bath) was solved to 2.8 Å resolution [30, 40]. The structure confirmed that pMMO is an $(\alpha\beta\gamma)_3$ homotrimer in which each αβγ protomer contains a single copy of the pmoB, pmoA, and pmoC subunits arranged as a 3-fold cylinder with a channel through the middle of the barrel (Figure 2). The pmoC and pmoA subunits comprise the bulk of the transmembrane region, which is ~45 Å in length. The N- and C-terminal cytosolic domains of the pmoB subunit have a cupredoxin-like β-barrel fold and are linked by two transmembrane helices. The global structure is highly consistent with earlier

cryo-electron microscopy images at 23 Å of *M. capsulatus* (Bath) pMMO [41]. The electrostatic surfaces of the pmoB cupredoxin domains are strongly negative and may facilitate docking to methanol dehydrogenase (MDH) [42], the second enzyme in the methane catabolic pathway.

2.2 Metal Centers

The initial *M. capsulatus* (Bath) pMMO structure identified three metal binding sites and a fourth hypothetical site derived from a clustering of potential metal ligands. At each of the occupied sites, the type of bound metal was identified by anomalous difference electron density maps [30]. The cytosolic domains of pmoB harbor two of these sites. On the N-terminal domain, His33, His137, and His139 and the N-terminal amine of His33 coordinate a dinuclear copper site located close to the membrane surface (Figure 3).
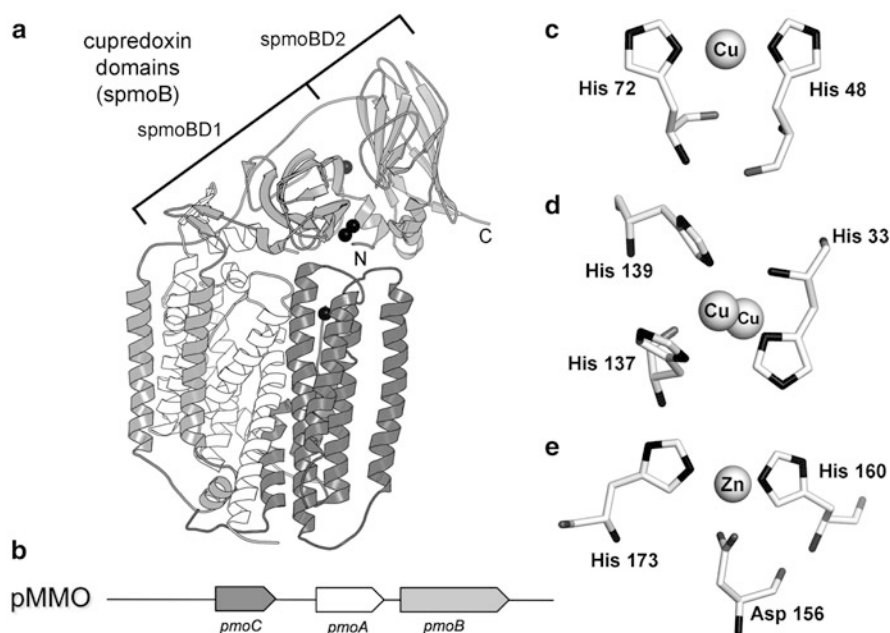
Figure 3 (**a**) The structure and subunit organization of a single pMMO αβγ protomer depicting the pmoA (white), pmoB (light gray), and pmoC (dark gray) subunits. The metal centers are shown as black spheres and from top down are the copper, dicopper, and zinc sites. (**b**) Organization of the pMMO operon. (**c**) Mononuclear copper site between the cupredoxin domains of pmoB. (**d**) Dinuclear copper site at the N-terminus of pmoB. (**e**) Zinc binding site in pmoC.

These residues are conserved across all known Proteobacterial methanotroph pmoB sequences [5]. Verrucomicrobia, which represent a distinct phylum of methanotrophs having pMMO-like sequences that are divergent from the Proteobacterial ones, do not conserve any of the ligands contributing to this site [5, 43]. It is unknown whether the Verrucomicrobia homologues oxidize methane or carry out an alternative function in these organisms. pmoB residues 1–32 are an N-terminal signal sequence that targets the protein to cytoplasmic membranes and they are cleaved off *in vivo* to facilitate assembly of the dinuclear site. The Cu−Cu distance was modeled at 2.5–2.6 Å based on X-ray absorption spectroscopy (XAS) data for the isolated protein [34, 44]. Similar Cu−Cu distances were observed in *M. trichosporium* OB3b and *Methylocystis* sp. strain M pMMO [39, 45]. At this resolution, finer details about the ligand geometry and identities of the exogenous terminal and bridging ligands could not be determined. Subsequent low resolution structures of pMMO from *M. trichosporium* OB3b (3.9 Å) and *Methylocystis* sp. strain M (2.68 Å) suffer from a similar problem that make it very difficult to definitively build an accurate representation of this dimetallic site [39, 45]. In the *Methylocystis* structure, two of the three centers are modeled with only one copper, suggesting how labile the metal ion may be at this site.

At the interface between the N- and C-terminal cupredoxin domains of the pmoB subunit of *M. capsulatus* (Bath), a mononuclear copper-binding site is coordinated by His48 and His72 (Figure 3c) [30]. Among homologous Proteobacterial and Verrucomicrobia pMMO proteins and the closely related ammonia monooxygenases, sequence alignments indicate His48 is not conserved and is replaced with either Asn, Gln, Thr, or Val [5]. *M. trichosporium* OB3b and *Methylocystis* sp. strain M pMMO substitute His48 for an asparagine and show no copper binding at this position in their structures [39, 45].

A third metal binding site was identified in the transmembrane region of the pmoA subunit facing the large inner channel of the pMMO trimer (Figure 3e). In the *M. capsulatus* (Bath) and *Methylocystis* sp. strain M pMMO structures, zinc, required for crystallization, binds the enzyme and is coordinated to Asp156, His160, and His173. The *M. trichosporium* OB3b pMMO structure, which did not require zinc for crystallization, has copper bound at this position, but it should be noted that this metal was added during purification. Although the residues at this site appear to be conserved across all species, there are lingering questions as to whether this site is biologically significant [5].

Lastly, in the initial pMMO structure from *M. capsulatus* (Bath), a fourth putative site unoccupied by metal ions was identified at the interface between the pmoA and pmoC subunits in the transmembrane region based on the localization of several hydrophilic His, Met, Glu, and Asp residues [30]. This region of the protein was hypothesized to house proposed trinuclear copper and diiron catalytic sites [12, 46]. A higher resolution *Methylosinus* sp. strain M pMMO structure later revealed that some of the transmembrane helixes in this region of the protein were mistraced in the original *M. capsulatus* (Bath) pMMO structure [39]. The resulting re-traced structure shows this fourth putative site to be non-existent.

2.3   Identifying the Active Site

2.3.1   Proposed Active Sites

Over the years, it has been a challenge to identify the location and metal content of the enzyme active site. Protein purifications from various laboratories yielding variable levels of copper atoms per protomer with and without 1–2 iron atoms produced spectroscopic data from which several different active site models were proposed [14, 33–39]. Early electron paramagnetic resonance (EPR) spectroscopic investigations of *M. capsulatus* (Bath) membrane fractions and purified protein containing 15–20 coppers per protomer yielded type II copper spectra with a hyperfine splitting pattern and an isotropic signal at $g = 2.06$ that were interpreted to suggest the existence of catalytic and electron transfer trinuclear copper centers with similar configurations to those of multicopper oxidases like laccase, ascorbate oxidase, and ceruloplasmin [47–50]. A similar type II Cu(II) EPR signal was observed in preparations from *M. trichosporium* Ob3b [51, 52].

Preparations of pMMO from *M. capsulatus* (Bath) and membrane fractions of *Methylomicrobium albus* BG8 from different laboratories, however, exhibited spectra more typical of type II Cu(II), which could be interpreted as a mononuclear copper site having a square planar composition and a coordination sphere comprising mostly histidines [33, 38, 53–55]. These findings, in addition to the purification and spectroscopic characterization of active pMMO with 2–3 copper atoms per protomer, called into question the plausibility of a trinuclear copper site [34, 44]. The first crystal structures of pMMO suggested that mononuclear and dinuclear copper centers should be considered carefully as the locus of catalytic activity, given their similarity to type II and type III copper centers in amino acid/peptide monooxygenases and catechol oxidase, respectively [40, 49].

Lastly, several laboratories, after accounting for a common cytochrome contamination, proposed pMMO to be an Fe–Cu enzyme, because pMMO preparations having higher iron content seemed to display better activity [12, 14, 38, 51, 56, 57]. Mössbauer spectroscopic study of purified pMMO fractions from *M. capsulatus* (Bath) containing significant levels of non-heme iron suggested the presence of a carboxylate-bridged diiron center similar to that in sMMO [57]. The three conserved residues that constituted the mononuclear zinc/copper site were proposed as the location for this iron center, despite the paucity of potential amino acid ligands, conserved or otherwise, needed to support a dinuclear site at this position.

The foregoing discrepancies between competing laboratories may have their origin in one or more of the following: differences in protein preparation leading to the loss of labile copper and/or iron; possible co-purification of pMMO with methanobactin, which would increase the amount of copper in the samples; contamination by the sMMO hydroxylase component (MMOH), which would add diiron centers; or the presence of bacteriohemerythrin, a hemerythrin-like protein expressed at high copper levels that is proposed to deliver O_2 to pMMO, which would also elevate iron levels [12, 27, 35, 46, 58].

2.3.2 Evidence for a Dicopper Active Site

Several lines of evidence indicate the dicopper site to be the locus of methane oxidation in pMMO. Metal reconstitution studies of apo-pMMO from *M. capsulatus* (Bath) revealed that the addition of 2–3 copper ions per protomer returned 90 % of the original activity whereas the addition of iron had no effect on turnover [39, 59]. Adding more than 2–3 equivalents of copper per apo-pMMO protomer inhibited the enzyme [60], possibly by hydrogen peroxide formation because the addition of catalase minimized this effect [61].

Studies of the *M. capsulatus* (Bath) pmoB cupredoxin domains provide the most significant line of evidence pointing toward the dicopper site as the one responsible for methane hydroxylation [60]. A recombinant soluble construct, termed spmoB, was created by replacing the two transmembrane helices anchoring the pmoB subunit to the membrane with a soluble synthetic linker that fused the two pmoB cytosolic domains (spmoBD1 residues 33–172 and spmoBD2 residues 265–414) (Figure 3a). After refolding the protein from inclusion bodies and reconstituting, spmoB bound ~3 copper ions and oxidized methane with an activity of 203.1 ± 20.2 nmol min^{-1}μmol^{-1} compared to that of the full length protein, 2290 ± 60 nmol min^{-1} μmol^{-1}. This result indicated that the cytosolic domains, and not the transmembrane region, are responsible for the hydroxylation chemistry. A His48Asn variant that removed the mononuclear copper site at the interface between the cupredoxin domains afforded a construct that bound ~2 coppers and displayed 10 % activity compared to that of the original spmoB. This decrease was attributed to a misfolding of the two domains, which share over ~1400 Å^2 of buried surface area. Conversely, a His137, 139Ala spmoB double variant targeting the dicopper site bound ~1 copper ion and all activity was abolished. XAS studies detailing the coordination environment around the copper centers of spmoB indicated three- to four-coordinate Cu(I) and an O/N rich environment with average Cu–O/N distances of 1.95 Å and a Cu–Cu interaction at 2.53 Å. These values are nearly identical to those obtained from fits to XAS data of purified and copper-reconstituted full-length pMMO.

The low activity of spmoB compared to the full length enzyme, while a concern, can be attributed to several factors. Not all of the protein may have been refolded properly, and delivery of electrons to the metal center may not be as efficient in the absence of the transmembrane domains. The dicopper site in the spmoB construct is highly solvent-exposed. It is conceivable that the transmembrane domains plus the lipid membrane play a significant role in coordinating reactivity of the reduced metal center with gaseous substrates so as to prevent buffer components from adventitiously quenching the reaction. In short, all signs point toward a dinuclear copper site as the likely pMMO active site. Although the location of the active site has become clarified, a detailed picture of the resting dimetallic center structure with the appropriate copper-coordinating protein- and solvent-derived ligands and their geometries remain to be determined. The square-planer 3–4 coordinate geometry indicated by EPR and XAS studies suggest that each copper at this site requires an additional 1–2 ligands [34, 53, 60], which presumably are solvent-derived oxo, hydroxo, and/or aqua species.

Beyond the residues that coordinate directly to the dicopper center, strictly conserved amino acids in the pmoB subunit in the second coordination sphere that could participate in O_2 and CH_4 activation process are scarce. Acidic residues at positions 339 and 35 in *M. capsulatus* (Bath) pMMO are intriguing candidates for further investigation into pMMO metal center assembly and proton transfer events, given their close proximity to the dicopper site (Figure 4a), but they are not conserved in related methanotrophs.
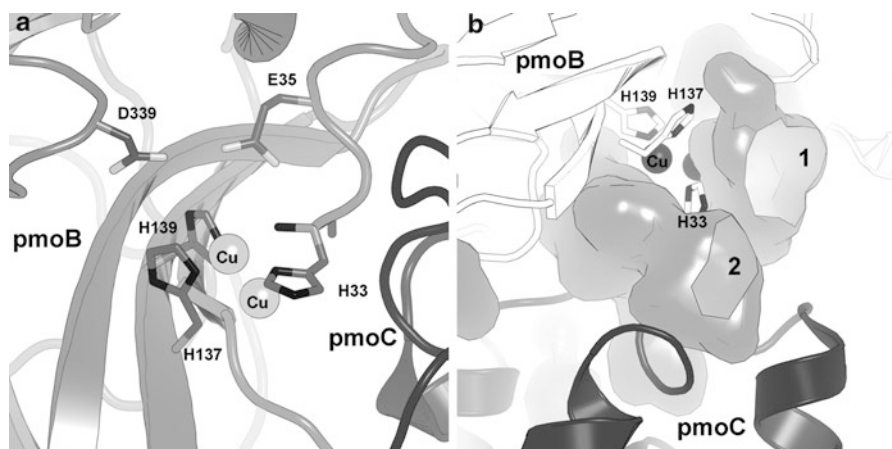
Figure 4 (**a**) Local environment surrounding the pMMO dicopper center. (**b**) Putative substrate-binding cavities (1 and 2) adjacent to the pMMO dicopper center. The pmoB and pmoC subunits are depicted as white and gray ribbons, respectively.

The absence of any conserved residues beyond those that coordinate to the metals stands in contrast to the situation for sMMO and related bacterial multicomponent monooxygenases (BMMs), where highly conserved residues in the second and third coordination spheres are essential for assembly of the hydroxylase diiron center, proton transfer (via conserved Thr213 and Asn214 residues), O_2 and methane access to the diiron center, as well as electron transfer.

2.4 Substrate Access and Product Egress from the Dicopper Site

2.4.1 Access to the Substrate-Binding Pocket

The pMMO dicopper site is located about 6 Å from the protein surface, almost at the interface between the transmembrane and cytosolic domains. Surface calculations show cavities on both faces of the dicopper center providing access to solvent through small openings in the protein surface (Figure 4b). Cavity 1 is

shallow (5–6 Å deep), lined with polar residues, and relatively solvent-exposed. Cavity 2 lies between the first pmoB cupredoxin domain and pmoC at the transmembrane interface. This cavity is longer (~14 Å), narrower, and quite hydrophobic. These features are conserved in three pMMO crystal structures, but the variable dicopper center geometries observed at low resolution make it difficult to visualize the exact morphologies of these pockets. The narrow substrate profile of pMMO, comprising short-chain alkanes of up to five carbons in length, and enantioselective formation of R-2-alcohols tends to support the latter sterically restricted cavity as the substrate-binding pocket [62–64]. It is unclear whether the wider more polar cavity has any function, although one could speculate that it might support the binding of membrane associated quinones and help to facilitate direct electron transfer from the reductant to the dicopper center.

2.4.2   Substrate and Product Channeling

The requirement of a 300 kDa protein for activating such small substrates suggests that the large scaffold may play a significant role in channeling and coordinating the movement of molecules to and from the active site. Additional "holes" noted in the exterior of the pMMO structure at the membrane interface may serve this purpose by controlling hydrocarbon and O_2 access to the dicopper center [41], possibly by using a scheme similar to that observed in the sMMO and its homologue, toluene/o-xylene monooxygenase (ToMO), where a series of hydrophobic cavities facilitate dioxygen movement through the protein [65]. Dioxygen delivery may also be conferred by bacteriohemerythrins [66]. Like pMMO, expression of this O_2-binding protein is up-regulated at high copper-to-biomass ratios. For *M. capsulatus* (Bath), enhanced hydroxylation activity occurs with the addition of bacteriohemerythrin to pMMO-enriched membranes, suggesting this component to be important for delivering dioxygen to the intracytoplasmic membranes.

A cryo-electron microscopy structure of pMMO detailing how MDH docks on top of the pmoB cupredoxin domains suggests the two proteins participate in substrate channeling, possibly by using the central cavity as a mode for product egress [41, 42]. Some biochemical evidence for channeling may come from work using the suicide substrate acetylene, which, when activated by the enzyme, covalently attaches to nearby amino acids by a mechanism that has yet to be fully resolved. Before the pMMO crystal structures were obtained, mass spectrometric analysis of ^{14}C-acetylene-labeled pMMO identified modified sites in the pmoA and pmoB subunits and suggested early on that the active site did not reside in the pmoB cupredoxin domain but instead in the other subunits [16, 38, 67]. Similar results were obtained with AMO, in which His191 in the AmoA subunit (the analog to Tyr186 in the *M. capsulatus* (Bath) pmoA subunit) was distinctly labeled [68–70]. This residue is ~14–19 Å removed from the pmoB dicopper center and sits close to the central cavity of the pMMO trimer. The modification of residues distant from the dicopper site suggests the activated acetylene compound migrates through the protein before it covalently attaches and that internal cavities may play a specific role in coordinating substrate and product movement.

2.4.3   Electron Sources

The source of electrons for the pMMO system is currently unknown. Membrane-bound quinols associated with the electron transport chain have long been assumed to be the pMMO reductants [33, 34, 38, 51]. This assignment is consistent with steady state experiments on isolated membranes or purified protein, which have successfully employed duroquinol as the reductant. Other laboratories have noted NADH-dependent activity [35], although it is likely that there was co-purification of pMMO with a type 2 NADH:quinone oxidoreductase contaminant [14].

Recent co-purification of pMMO with MDH led to a reconsideration of a hypothesis in which electrons from the oxidation of methanol are recycled into the oxidation of methane [42, 71]. It is possible that the reduced pyrroloquinoline quinone ($PQQH_2$) cofactor generated by oxidation of methanol to formaldehyde in MDH donates its electrons back to pMMO as the last step in its catalytic cycle. Such an event could obviate any need to shuttle NADH generated by downstream reactions through additional redox proteins to supply pMMO with reductant and facilitate faster growth. Further work is required to definitively establish the electron source.

2.5   Mechanism

A major goal for researchers working on pMMO is to provide a detailed understanding of its mechanism, and especially how pMMO is unique compared to other hydrocarbon-oxidizing dinuclear copper proteins like tyrosinase and catechol oxidase. The problems associated with the purification and stability of pMMO, as well as the controversy surrounding the identification of the active site, have slowed progress, especially when compared to our understanding of sMMO.

Complicating matters further is the difficulty in studying membrane proteins like pMMO with rapid kinetic and spectroscopic methodologies in order to observe key intermediates in the O_2 and C–H bond activation processes. Although information is scarce, some significant progress has been made recently toward this goal. Here we examine current knowledge of the O_2 and C–H bond activation steps in pMMO as well as additional insight gained by related work from model compounds and computational studies.

2.5.1   Spectroscopic Identification of an Oxygen Intermediate

The first, and currently only, observed spectroscopically detected intermediate in pMMO was identified by addition of anoxic hydrogen peroxide to ascorbate-reduced *M. capsulatus* (Bath) pMMO, which over 12 h produced a stable optical

feature at 345 nm with $\varepsilon = 10,000 \text{ cm}^{-1} \text{ M}^{-1}$ [72]. This same optical spectrum was observed in spmoB samples, but here it appeared almost immediately after reacting the reduced protein with either O_2 or H_2O_2. It is not understood why pMMO reacts differently than spmoB toward O_2 and H_2O_2, but greater substrate accessibility to the active site in spmoB was suggested to play a role. As expected, the spmoB His48Asn variant behaved like the wild-type spmoB and the His137, His139 double variant exhibited no reactivity toward dioxygen or hydrogen peroxide, again identifying the dicopper site as the essential catalytic center. The addition of methane to this stable copper-oxygen complex in pMMO and spmoB results in a disappearance of the spectral feature, demonstrating that this oxygen-derived intermediate is catalytically competent and possibly the one responsible for C–H bond activation. The optical spectroscopic properties of the pMMO oxygen-derived species have been observed in type III copper systems like tyrosinase, hemocyanin, and multicopper oxidases, and these are characteristic of either a $\mu\text{-}\eta^2\text{:}\eta^2$-peroxo Cu_2^{II} or a hydroxo-bridged Cu_2^{II} intermediate (Table 1) [73–76].

Table 1 Spectroscopic Parameters of Dicopper-Oxygen Complexes.

	Optical		Cu–Cu (Å)	Cu_2^{II}/O_2 Species
	λ_{max} (nm)	ε (M^{-1} cm^{-1})		
pMMO, spmoB [5]	345	10,000		
Oxyhemocyanin [74]	350; 580	20,000; 1000	3.6	$\mu\text{-}\eta^2\text{:}\eta^2$
Oxytyrosinase [74]	350; 580	18,000; 1000	3.4	$\mu\text{-}\eta^2\text{:}\eta^2$
Met-hemocyanin [74]			3.1	di-μ-hydroxo
Multicopper oxidases [73]	330	5000	3.7	μ-hydroxo

The dinuclear metal centers in these related type III copper proteins are coordinated by 5–6 histidines, have much longer Cu–Cu distances of 3.1–3.6 Å, and appear more constrained by the surrounding protein scaffold. By contrast, the bidendate coordination of one copper in pMMO by the N-terminal histidine may offer greater flexibility and allow the metal center to adopt novel geometries that have yet to be identified. The exact structure of the pMMO intermediate remains uncertain, however, and further structural and biochemical characterization of this species is crucial to further our understanding of the enzyme chemistry. Unfortunately, the application of resonance Raman spectroscopy is limited by the presence of a persistent cytochrome contaminant in purifications of the native protein, and high concentrations of refolded spmoB have been difficult to achieve.

2.5.2 Computational Studies and Comparisons to Copper Model Compounds

Computational studies examining the reactivity of O_2 and CH_4 with the different copper sites in pMMO and the characterization of copper model complexes have provided valuable insights into the pMMO mechanism [46, 77–79].

In one particular set of calculations, a mixed-valent di-μ-oxo-$Cu^{II}Cu^{III}$ species was found to be more reactive toward methane than either a mononuclear Cu^{III}-oxo or a di-μ-oxo Cu_2^{III} intermediate [77, 78]. Such a reactive di-μ-oxo-$Cu^{II}Cu^{III}$ center could be generated in the enzyme if an electron were injected into either a μ-η^2:η^2-peroxo Cu_2^{II} or a di-μ-oxo Cu_2^{III} precursor, although the latter species has yet to be identified in biological systems [4, 80] (Figure 5). This electron could originate from a metal center, an exogenous reductant, or a protein residue. Methane oxidation by the reactive di-μ-oxo-$Cu^{II}Cu^{III}$ center was calculated to occur through a concerted, non-radical oxygen insertion mechanism (Figure 6).
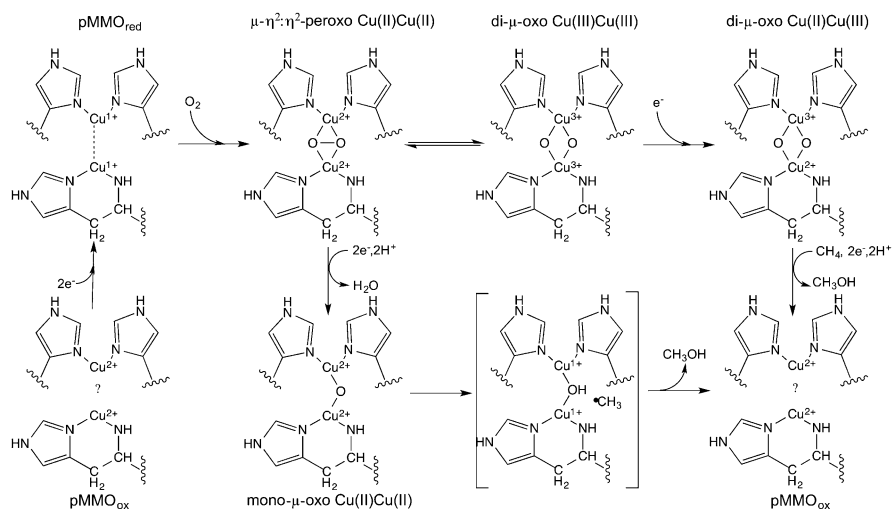
Figure 5 Proposed mechanisms for O_2 activation by pMMO. Figure adapted from [4].

A possibly significant development in the pMMO field was the identification of a copper zeolite, Cu-ZSM-5, that readily oxidizes methane to methanol at 100 °C [81]. Mechanistic characterization of this complex revealed that O_2 binding first results in a μ-η^2:η^2-peroxo Cu_2^{II} complex followed by subsequent conversion to a reactive bent mono-μ-oxo-Cu_2^{II} species [82–84]. Electrons for the process are proposed to come from spectator Cu^I ions in the zeolite. DFT calculations on this compound suggested the C–H activation step occurs at the bridging oxygen, resulting in a transient $[Cu–OH–Cu]^{2+}$ intermediate and methyl radical that rapidly recombines with the copper-bound hydroxyl radical to form methanol (Figures 5 and 6). Until further characterization of pMMO is carried out, it is unknown which, if any, of these mechanistic possibilities accurately represent the O_2 activation events and the essential catalytic intermediate in the enzyme.

Figure 6   Radical and concerted mechanisms of C–H bond activation. M represents the reactive metal in either pMMO or sMMO.

2.5.3 Mechanism of C–H Bond Breaking

The C–H bond activation steps in pMMO and sMMO have been examined by using substrate probes to differentiate between cationic, alkyl radical, or concerted oxygen insertion mechanisms (Figure 6). These probes generally fall into two classes, chiral substrates and radical clock probes, the latter of which are too large to be accommodated by the pMMO active sit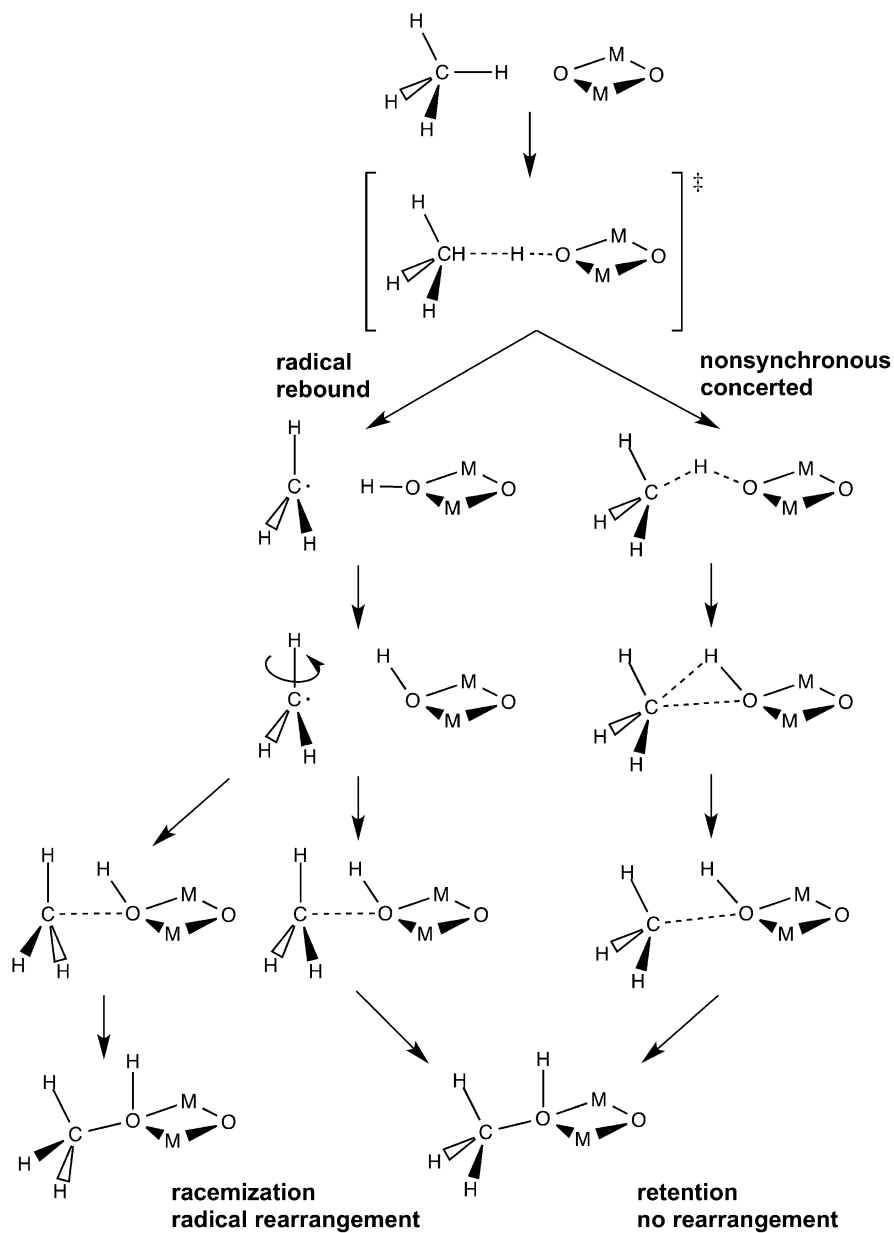e. Reactions of pMMO with the (S) or (R)-[1-^{3}H$_1$,^{2}H$_1$] ethane and [2,2-^{2}H$_2$] butane assessed the reactivity of pMMO toward a chiral methyl group [27, 85, 86]. An inversion of configuration suggested rotation about the C–C bond of a radical or cationic ethyl intermediate. The calculated lifetime of such an intermediate, given the barrier of C–C bond rotation in an ethyl radical (0.15 kcal mol^{-1} at 30 °C), is ~180 fs [85]. Reactions with *M. capsulatus* (Bath) pMMO revealed complete retention of configuration, suggesting a concerted mechanism in which an oxygen atom is inserted between the C–H bond of a pentacoordinated species having either a C–O or C–Cu bond. A radical or cationic rebound mechanism exhibiting complete retention would have to occur faster than 10 fs in order to avoid detectable C–C bond rotation. This latter scenario is not feasible because it would require that radical capture be faster than the calculated rate constant for the decay of the transition state (6.6×10^{12} s^{-1} at 45 °C). However, given that pMMO has a narrow substrate-binding pocket, a mechanism invoking a bound radical with highly restricted rotation cannot be ruled out.

2.6 Unresolved Questions

Despite the progress made in the last 15 years, there are numerous unresolved questions concerning the structure and mechanism of pMMO. There is a great need for higher resolution structural data to further define the geometry and the solvent contributions to the resting dicopper active site. A better starting place for thinking about the pMMO mechanism is required, especially for those pursuing synthetic catalysts, model complexes, and computational studies.

Similarly, improvements in purification of both native pMMO and the spmoB construct are needed to facilitate more extensive mechanistic studies using time-resolved spectroscopic methods. Further insight into the structure of the long-lived peroxo species and discovery of new intermediates along the reaction pathway will provide a stronger framework for zeroing in on a mechanism for O$_2$ and C–H bond activation by this unique dicopper center. Finally, it is unknown how the requisite substrates are assembled at the metal center with appropriate timing in order to achieve efficient coupling of the different chemical processes. Resolving this question requires better understanding of the role of the large protein scaffold into which the dicopper unit is embedded and how both substrates and products are channeled to and from the active site in a controlled fashion. Much important work remains to be done.

3   Soluble Methane Monooxygenase

3.1   Genetics and System Components

3.1.1   Soluble Methane Monooxygenase

Soluble methane monooxygenase is a three-component enzyme system requiring a 251-kDa hydroxylase MMOH (*mmoXYZ*), a 38-kDa reductase MMOR (*mmoC*), and a 16-kDa regulatory or effector protein MMOB (*mmoB*) for optimal activity (Figure 7) [8, 10]. MMOH takes the form of an $(\alpha\beta\gamma)_2$ heterodimer and houses the carboxylate-bridged diiron active site ~12–14 Å below the surface of the hydroxylase α-subunit. MMOR, a [2Fe-2S]- and FAD-containing reductase, supplies electrons to the hydroxylase by consuming NADH. MMOB, a cofactorless protein, up-regulates activity by binding to the hydroxylase α-subunit near the diiron center to induce changes in the protein architecture that efficiently couple NADH consumption with substrate oxidation.
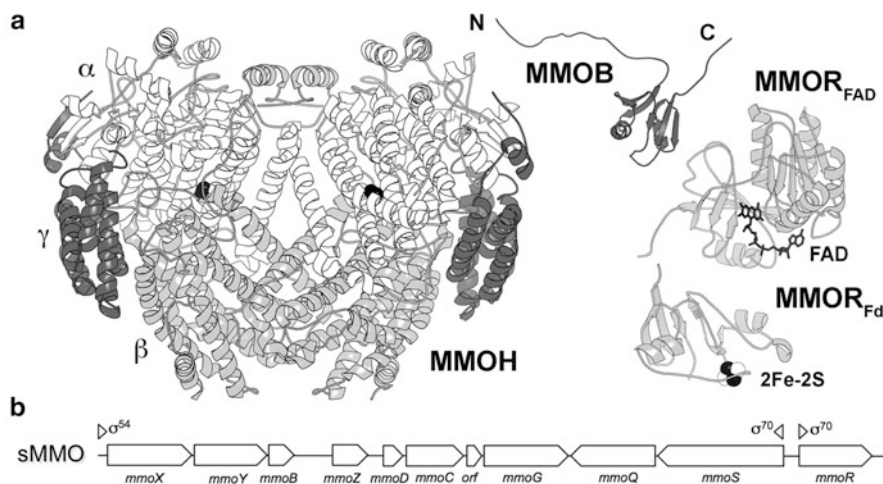
Figure 7 (**a**) sMMO components. (**b**) sMMO operon from *M. capsulatus* (Bath).

The sMMO operon from several methanotrophs has been sequenced and contains additional genes that are hypothesized to encode for proteins important for controlling expression and assembly of the system (Figure 7b) [87–90]. In the middle of the catalytic gene sequences is *mmoD* (formerly *orfY*), which encodes for a protein of unknown function (MMOD) and inhibits sMMO activity by competing with MMOB for the same binding site on MMOH [91, 92]. Comparisons to DmpK (also known as PHK) in related phenol hydroxylase systems have suggested that MMOD could play a role in the metal center assembly of MMOH, although this hypothesis has yet to be proved. MMOD has also been proposed to serve as a transcriptional regulator of the sMMO operon [93]. Downstream of the sMMO genes are *mmoQ*, *mmoS*, *mmoR* and *mmoG*. The *mmoR* gene encodes for a

σ54-dependent transcriptional activator thought to control the copper-dependent expression of sMMO. MMOQ and MMOS, which show significant homology with two-component sensor-regulator systems, have been proposed to activate the σ54-dependent transcriptional activator, but exactly how these proteins sense the cell environment and interact has yet to be established [87, 94, 95]. Lastly, MMOG is a putative GroEL-like protein-folding chaperone that may facilitate proper assembly of MMOH and the transcriptional activator [87, 89, 96]. The organization and composition of the sMMO operon varies among the different methanotrophs.

Given the complex structure of MMOH and the extra genes required for its assembly, it is not surprising that no one has yet generated a robust heterologous expression system for the hydroxylase despite numerous attempts and claims. Consequently, almost all studies on MMOH have been conducted on native protein purified from either *Methylococcus capsulatus* (Bath), a thermophile with an optimal growth temperature at 45 °C, or *Methylosinus trichosporium* OB3b, a mesophile with optimal growth at 30 °C. The hydroxylase components from other BMMs, such as toluene 4-monooxygenase, (T4MO), toluene/o-xylene monooxygenase (ToMO), and PH (phenol hydroxylase), have been recombinantly expressed in *E. coli* [97–99]. These alternate systems allow conserved residues and structural features within these proteins to be probed by mutagenesis. Thus, some of the ideas about sMMO function presented below rely on analysis of and comparisons to related BMM systems.

3.1.2   Related Bacterial Multicomponent Monooxygenases and Substrate Specificities

sMMO is the most well characterized member of a larger family of bacterial multicomponent monooxygenases that can be subcategorized into sMMO/alkane monooxygenases (MMOs), four-component alkene/aromatic monooxygenases (TMOs), phenol hydroxylases, alkene monooxygenases (AMOs), tetrahydrofuran monooxygenases (THFMOs), and hyperthermophilic aromatic/alkene monooxygenases [100, 101]. Enhanced environmental screening and genomic sequencing have expanded the diversity and scope of these subfamilies since the genetics were last reviewed [101]. All of these systems utilize the same protein components, a hydroxylase, a regulatory protein, and a reductase. Members of the four-component toluene monooxygenases require both a flavin and Rieske protein to shuttle electrons to the hydroxylase. These different systems, which evolved to hydroxylate or epoxidize specific hydrocarbons for efficient carbon and energy assimilation in lower metabolic pathways, have relatively flexible substrate binding pockets that accommodate numerous alternate substrates.

The hydroxylase α-subunits are the most conserved among the different classes and share ~21–35 % sequence identity to MMOH and related alkane monooxygenases. Even though the residues that contribute to the assembly of the diiron center are conserved and the active site structures of related family members are similar, if not identical, to that of MMOH [102–104], none of these other systems can hydroxylate methane. sMMO is a special member of this enzyme

class. Even the 65 % identical butane monoxygenase cannot activate methane [105], suggesting there are highly relevant and fundamental structure function relationships between the metal center and protein scaffold that are essential for tuning reactivity toward small alkanes.

3.2   Component Structures and Function

3.2.1   Soluble Methane Monooxygenase Hydroxylase

The 251-kDa hydroxylase component is an $(\alpha\beta\gamma)_2$ heterodimer with a 2-fold axis of symmetry (Figure 7) [106, 107]. A large canyon is formed at the interface between the $\alpha\beta\gamma$ protomer in the middle of the molecule that is important for the docking of the other protein components. The diiron center is located in the α-subunit and housed within a four-helix bundle comprising helices B, C, E, and F, the latter two of which form a surface of the canyon that is critical for binding MMOB and undergo helical rearrangements upon protein component binding (Figure 8) [108]. The remainder of
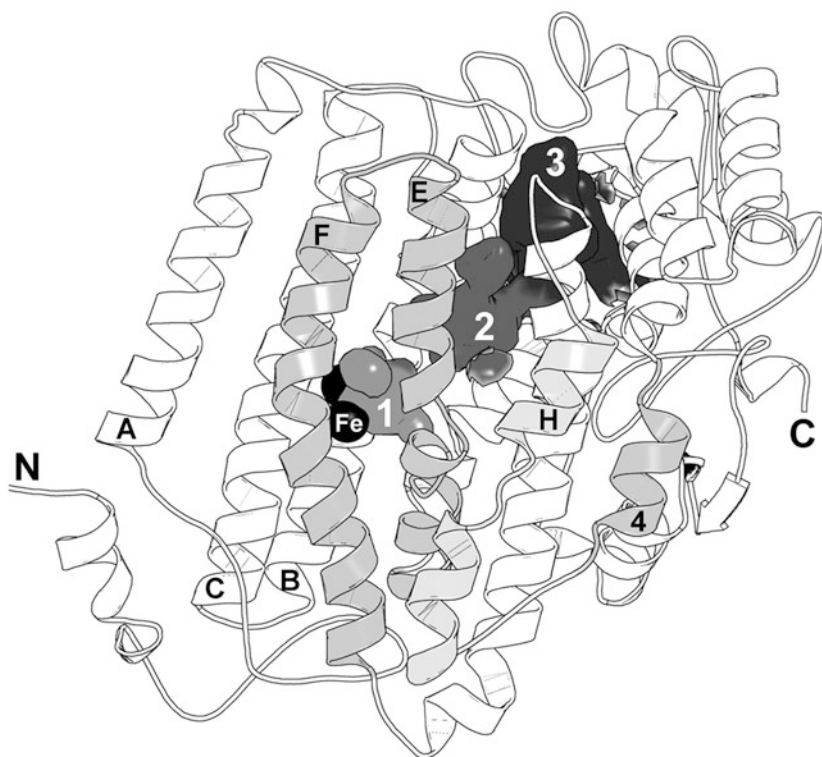

Figure 8   sMMO α-subunit depicting the hydrophobic cavities (1, 2, and 3). Iron atoms are shown as black spheres. Helices E, F, H, and 4, which are the primary MMOB docking surfaces on MMOH, are shaded light gray.

the protein, particularly the α-subunit, plays an important role in coordinating the efficient assembly and activation of the different substrates (electrons, protons, hydrocarbon, and dioxygen) at the active site using a series of hydrophobic cavities, hydrogen bonding networks, and electron transfer pathways (Figure 8) [109, 110].

At different times during the reaction cycle, MMOB and MMOR dock on to MMOH and induce changes in MMOH that are not only responsible for activating the diiron center, but may also help to coordinate the catalytic events [111]. The hydroxylase can accommodate the binding of two molecules of MMOB and MMOR, one on each face of the hydroxylase. Optimal activity in *M. capsulatus* (Bath) MMOH, however, is observed with a 1:2:0.5 H:B:R ratio, suggesting that MMOR binds transiently to the hydroxylase and services multiple diiron centers [111]. In the absence of MMOB, MMOH functions primarily as an NADH oxidase. More details about the specific effects of each component, the shuttling of substrates, and the coordination of catalytic events are discussed below.

3.2.2   The Reductase and Electron Transfer to the Hydroxylase

MMOR is a typical reductase with an N-terminal [2Fe-2S] ferredoxin ($MMOR_{Fd}$) domain and a C-terminal FAD-binding ($MMOR_{FAD}$) domain. NMR structures of the individual domains from *M. capsulatus* (Bath) are available [112, 113] (Figure 7). Electron transfer kinetics in the sMMO systems have been investigated in detail by using stopped-flow optical spectroscopy [114–117] (Figure 9).
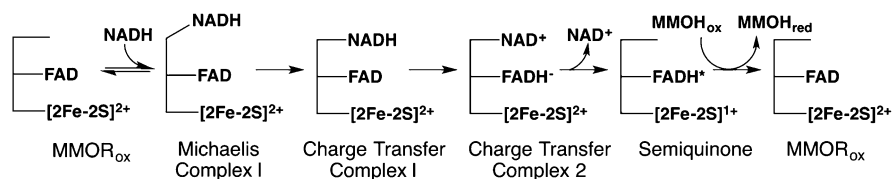
Figure 9   Electron transfer steps from MMOR to $MMOH_{ox}$. The figure was adapted from [8].

Briefly, after the binding of NADH to the $MMOR_{FAD}$ domain, the first electron transfer event produces the two-electron reduced FAD hydroquinone ($FADH^-$) and NAD^+. Following the release of NAD^+, a one-electron transfer step produces the flavin semiquinone ($FADH^•$) and the reduced [2Fe-2S] intermediates. Two successive electron transfer steps ultimately yield the reduced hydroxylase, $MMOH_{red}$. The reduction potentials of the MMOR cofactors are not affected by the hydroxylase or the regulatory protein [117].

3.2.3   The Regulatory Protein and Interactions with the Hydroxylase

MMOB is organized into a structured 95 amino acid core with flexible N- and C-terminal tails of 35 and 11 amino acids, respectively [118, 119] (Figure 7). A newly available structure shows that it docks onto the MMOH α-subunit in the

canyon region on top of helices E and F, which contribute glutamate and histidine ligands to the diiron center (Figure 10) [108]. The protein enhances the steady state reactivity of sMMO by 8–150 fold [108, 120], accelerates the rate of O_2 activation by the reduced metal center by 1000-fold [121], efficiently couples NADH consumption to substrate hydroxylation, alters the spectroscopic and redox properties of the diiron center, and influences the regio- and stereospecificity of the sMMO-catalyzed reaction [8, 10, 122]. Similar phenomena are observed in the other BMM systems [122–124]. A long-standing goal is to understand how the structural changes that shift the relative population of hydroxylase molecules into an active conformation account for the altered properties of the activated enzyme. The specifics of these changes in relation to sMMO activation are discussed in Section 3.4.2.
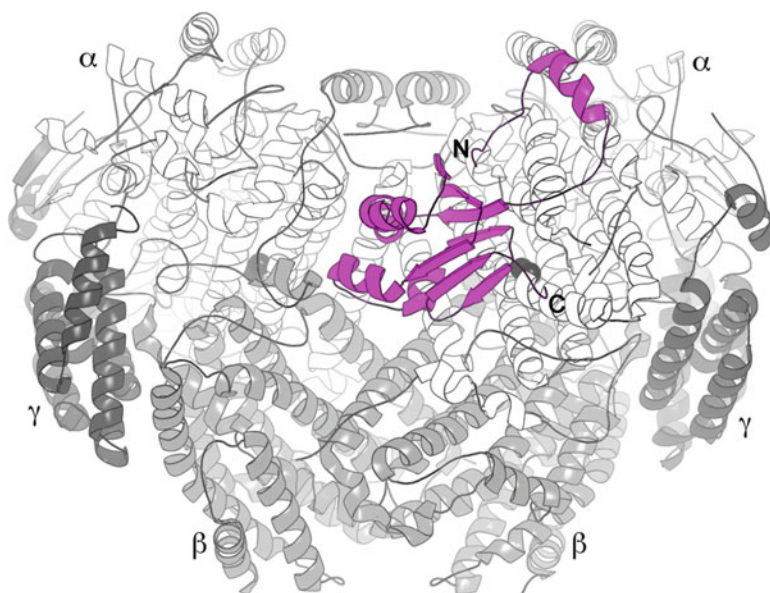
Figure 10 Structure of the MMOH-MMOB complex (PDB entry 4GAM). MMOB is colored magenta.

Also relevant to the activation process are contributions from the MMOB N-terminus that forms a ring-like structure when docked onto the surface of the MMOH α-subunit [108]. Removing residues from the N-terminus yields protein forms that have slightly diminished affinity for MMOH with significant loss of activity [108, 125–127]. Nevertheless, a N-terminal truncate of MMOB lacking the first 12 residues failed to alter the redox potentials of the hydroxylase diiron center [125]. The combined data indicate the MMOB N-terminus is essential for the regulatory protein to trigger important structural changes in MMOH required for activity. Similarly, MMOB C-terminal deletions have measurable effects on reaction rates and the efficient formation of sMMO intermediates [128].

3.3   The Diiron Center

The MMOH carboxylate-bridged diiron center has been the subject of numerous spectroscopic and structural investigations to ascertain how this metal unit activates dioxygen and hydrocarbons. These experiments, conducted in the presence and absence of the other protein components, substrates, products, and other chemical probes, have provided a considerable amount of information, not all of which is directly relevant to the focus of this chapter on catalysis. As the different mechanistic aspects are discussed, it is important to remember that it was the X-ray crystal structure of MMOH in the resting diiron(III) state (MMOH$_{ox}$), solved in the *absence* of MMOB, that provided the foundation for interpreting much of the data relevant to the sMMO catalytic cycle (Figure 11).
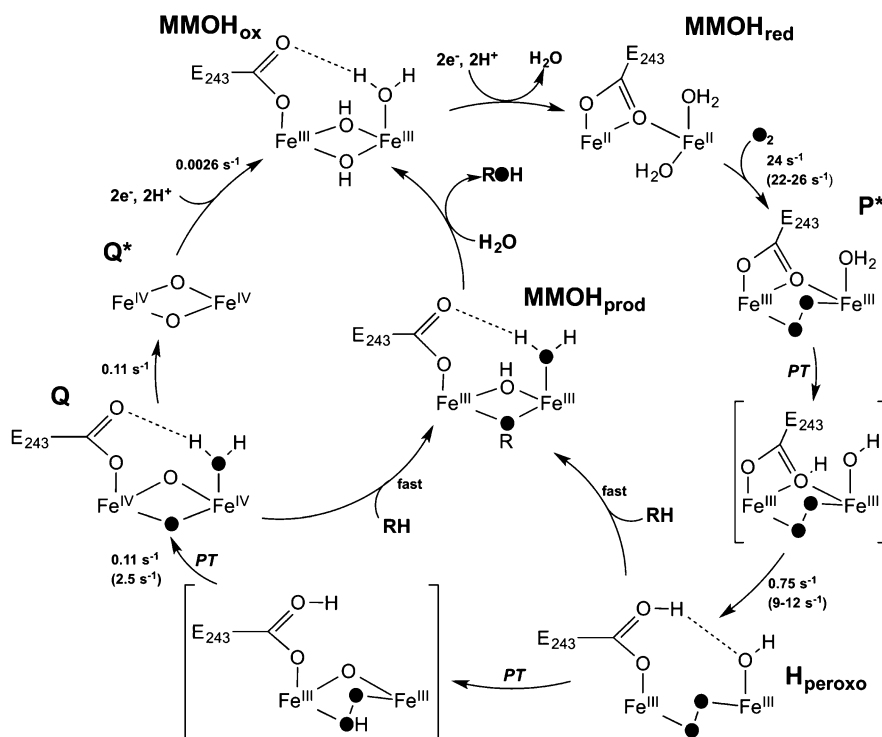
Figure 11   sMMO reaction cycle and intermediates. Proton transfer steps (PT) and rate constants for the *M. capsulatus* Bath and (*M. trichosporium* OB3b) systems are provided. P*, H$_{peroxo}$ = diiron(III) peroxo intermediates; Q, Q* = diiron(IV) intermediates.

The oxidized (MMOH$_{ox}$) and reduced (MMOH$_{red}$) forms of MMOH are the most stable and therefore have received the most structural and spectroscopic scrutiny. The one-electron reduced mixed-valent Fe^{II}Fe^{III} diiron center (MMOH$_{mv}$), while stable, is not an intermediate in the cycle. MMOH$_{mv}$, however, is EPR-active and has been useful for interrogating aspects of the sMMO system.

3.3.1   The Oxidized Hydroxylase

MMOH$_{ox}$ has two high-spin Fe^{III} ions that are coordinated by four glutamates and two histidines (Figure 12a) [107, 129, 130]. The iron atoms lie ~3.0–3.1 Å apart and are bridged by two solvent derived hydroxide ligands, which antiferromagnetically couple the iron ions and lead to a diamagnetic ground state with a characteristic Mössbauer spectrum [131–134]. Glu243 shows the most positional variability in the different X-ray structures of MMOH$_{ox}$. It forms hydrogen bonds to either the terminal water on Fe1 or the bridging hydroxides [130].
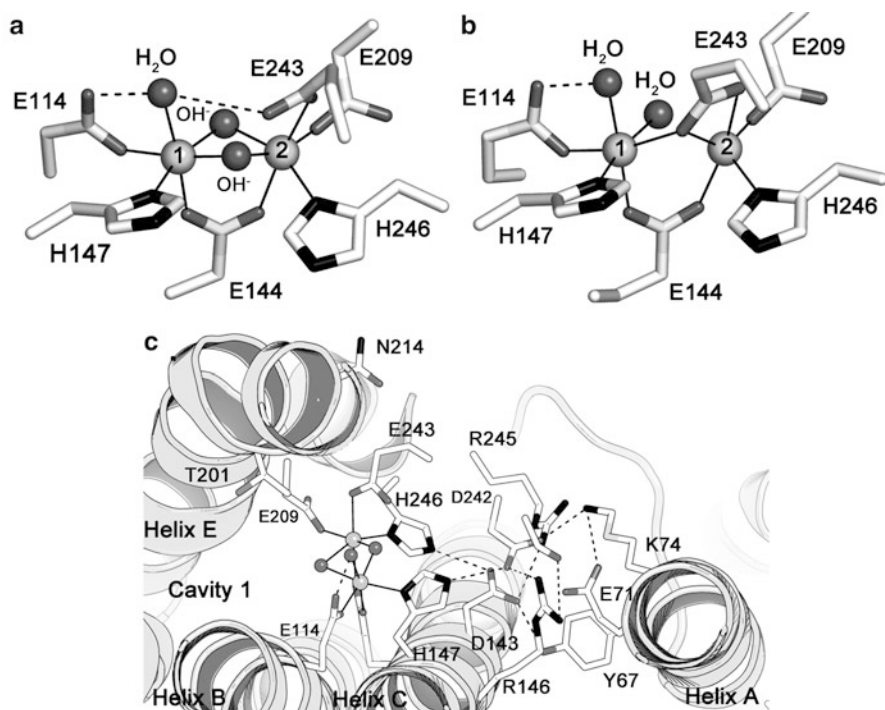
Figure 12 Structures of the (**a**) oxidized (PDB entry 1MTY) and (**b**) reduced (PDB entry 1FYZ) MMOH diiron centers in the absence of MMOB. (**c**) Conserved hydrogen bonding network behind the diiron center leading toward the canyon surface (PDB entry 1MTY). The nitrogen and oxygen atoms are colored black and gray, respectively.

The hydrophobic substrate-binding pocket lies distal to the coordinating histidines in front of the bridging hydroxide. Behind the diiron center, leading 10 Å from the histidine residues to helix A on the canyon surface of the hydroxylase, is an extensive hydrogen bonding network that is strictly conserved among the different BMMs (Figure 12c). The network may assist in the assembly of the diiron center. Functional roles, such as involvement in electron transfer, have yet to be established.

3.3.2   The Reduced Hydroxylase

Upon reduction of MMOH to the diiron(II) state (MMOH$_{red}$), both hydroxides are protonated to generate water, one of which is displaced when Glu243 undergoes a carboxylate shift to bind in a bridging, bidentate chelating mode to Fe2 (Figure 12b) [129, 130]. The remaining water stays coordinated to Fe1 and binds weakly to Fe2, based on the longer Fe–O distance. As a result of these changes, the Fe–Fe distance increases to 3.3–3.4 Å [135], and a possible coordination site opens up on Fe2. MMOH$_{red}$ is a weakly ferromagnetically coupled high-spin system with a characteristic EPR signal at $g = 16$ [132, 134, 136–138]. This EPR signal has been valuable for tracking the reaction of MMOH$_{red}$ with O_2.

Additional conformational changes of interest occur near the active site when MMOH$_{ox}$ is reduced in the absence of MMOB. Asn214, which sits above the diiron center on helix E, undergoes a rotamer shift from the protein surface to the interior (Figure 13) [130].
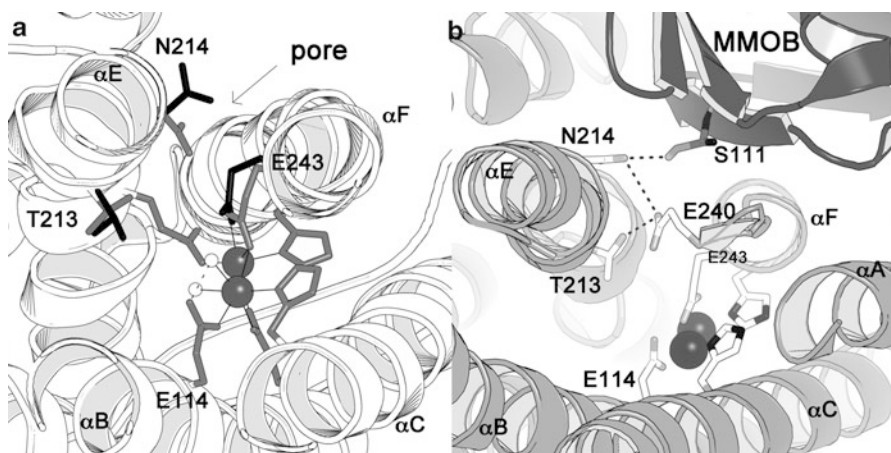
Figure 13 (**a**) The effects of redox state on the configuration of Thr213, Asn214, and Glu243 in MMOH. The side chains in MMOH$_{ox}$ and MMOH$_{red}$ are denoted as black and gray sticks, respectively. (**b**) Hydrogen bonding pattern between Thr213, Asn214, and Glu240 when MMOB is bound to the hydroxylase surface. The nitrogen and oxygen atoms are colored black and gray, respectively.

This shift most likely occurs because reduction breaks water-mediated hydrogen bonding interactions between Glu243 and Asn214. Such a mechanism suggests how movement of residues at the diiron center can trigger conformational changes on the protein surface. The rotamer change in Asn214 leads to the formation of a small pore from the surface to the active site that has been proposed as pathway by which hydrocarbons, dioxygen or protons can access the metal center or by which hydrophilic products like water and alcohols may leave [109, 110]. The structure of the MMOH-MMOB complex, however, reveals that MMOB docks to the hydroxylase on top of the pore and forms a hydrogen bond directly to Asn214 via its conserved residue, Ser111 (Figure 13b) [108]. A similar interaction occurs in structures of related BMM complexes [103, 104]. The exact function of Asn214 in sMMO and other BMM homologues is under investigation.

3.4 Protein Component Complexes

Understanding the interactions of MMOR and MMOB with the hydroxylase is essential for unraveling how sMMO efficiently performs its challenging catalytic task. Complexes formed between the different protein components play crucial roles in orchestrating the electron transfer, oxygen-activation, and hydrocarbon-activation events at the MMOH diiron center. Broadly stated, MMOR and MMOB can be viewed as having two very general regulatory functions, to control the movement of substrates to the active site and to alter the hydroxylase structure in such a way as to make the diiron center more reactive. How the components accomplish these tasks remains a focus of intense investigation.

3.4.1 Reductase Binding and Effects on the Hydroxylase

Initial chemical cross-linking studies between *M. trichosporium* (OB3b) MMOR and MMOH indicated that the reductase binds to the β-subunit [120]. More recent cross-linking studies on *M. capsulatus* (Bath) using just the $MMOR_{Fd}$ domain suggest that the primary interaction is actually with the MMOH α-subunit [139]. Spectroscopic studies of the MMOR-MMOH complex have shown that the reductase does not significantly influence properties of the hydroxylase diiron center [8], however, both MMOR and MMOB alter the redox potentials of MMOH [125, 131, 140–143]. Although there is some debate in the literature over their exact values, the general trends reflecting the effects of the different components on the MMOH redox potentials are consistent. Binding of MMOB decreases the potentials of the diiron center by ~100–200 mV, making it harder to reduce, whereas the docking of MMOR restores the potentials to the level observed before MMOB binding to MMOH to favor reduction. These changes are consistent with recent results indicating that MMOB displaces MMOR when it binds to MMOH [144].

Important questions concerning electron transfer in the sMMO system are where MMOR docks to MMOH and what is the electron transfer pathway through the hydroxylase to the diiron active site. An application of Marcus Theory to the electron transfer rates between $MMOR_{Fd}$ and MMOH estimates that the [2Fe-2S] cluster rests ~11–14 Å from the dinuclear iron center [114]. This distance is consistent with theories of efficient electron transfer rates in biological systems that generally position electron donors and acceptors within 14 Å of each other [145]. It should be noted that MMOB and MMOR do not form complexes with one another. Although it was previously suggested that they do not compete for the same binding site on MMOH [111, 120], the most recent studies indicate otherwise. In particular, they demonstrate that the MMOR Fd [Fe$_2$S$_2$] cluster docks near MMOH residues N214 and E240, the latter of which undergoes a conformational change that can facilitate the shuttling of both protons and electrons to the diiron center [144, 204]. MMOB, however, has a higher affinity for $MMOH_{red}$ than $MMOH_{ox}$ and can displace MMOR from the reduced hydroxylase. Consequently, MMOB can regulate the electron transfer process and possibly serve to prevent the quenching of the activated oxygen intermediates by MMOR.

3.4.2 Hydroxylase Activation by the Regulatory Protein

Before its crystal structure was determined, extensive spectroscopic interrogation of the MMOH-MMOB complex indicated that MMOB affects the electronic properties of the diiron center but alters its structure little. Correlating specific electronic changes with concrete structural modifications has been difficult, especially when trying to ascertain the structures of the different intermediates in the catalytic cycle. XAS studies of oxidized and reduced MMOH from *Methylococcus capsulatus* (Bath) and *Methylosinus trichosporium* (OB3b), which offer the most direct method for probing changes in coordination geometry, ligand type and number, and metal-ligand distances in the absence of a crystal structure, indicated that MMOB had no remarkable affect on the spectra or fitting parameters of $MMOH_{ox}$ or $MMOH_{red}$ [135, 146]. The only notable difference was that the Debye-Waller factors, a measure of thermal order for a fit atom, decrease [147]. This finding suggested that binding of the regulatory protein to the hydroxylase serves to limit the motion of the metal coordinating ligands.

EPR spectroscopic investigations of $MMOH_{ox}$ that was cryo-reduced at 77 K by γ-radiation to produce an EPR active mixed-valent $Fe^{II}Fe^{III}$ dimetallic center that maintains the structure of $MMOH_{ox}$ revealed that the addition of MMOB has no observable affect on the oxidized diiron(III) cluster [148]. In the presence of products like methanol and phenol, however, spectral changes in γ-irradiated $MMOH_{ox}$ occur when MMOB is added and indicated that MMOB influences the manner by which exogenous ligands bind to the metal center. Consistent with this notion is the observation that MMOB promotes DMSO and glycerol coordination to $MMOH_{ox}$, whereas in the absence of MMOB, the binding of these compounds is undetectable. MMOB also induces a spectral change in the $g = 1.84$ EPR signal of chemically reduced $MMOH_{mv}$, indicating that MMOB can alter the magnetic coupling of the metal center [120]. For $MMOH_{red}$, the characteristic $g = 16$ EPR signal of fully reduced hydroxylase is not altered significantly in the presence of MMOB [120, 132, 133, 136, 137].

Further investigation of $MMOH_{red}$ by circular dichroism (CD) and magnetic circular dichroism (MCD) spectroscopy demonstrated that MMOB influences the structure of the fully reduced diiron center by altering the ligand field environment of only one of the iron atoms [149, 150]. The ligand field environment of the second iron atom only changes when MMOB is bound to MMOH in the presence of substrates and inhibitors. Although it is unknown which specific iron atom experiences these different effects, the data appear consistent with EPR results suggesting that MMOB helps to generate open coordination sites at the diiron center for dioxygen activation [149, 150]. Rapid freeze quench (RFQ) EPR spectroscopic experiments reveal that MMOB increases the rate of O_2 association with the enzyme by 1000-fold, which corroborates this assessment and demonstrates how MMOB can either accelerate the formation of intermediates or facilitate dioxygen access to the active site [121]. The structural changes observed in the MMOH-MMOB complex tend to support the latter function [108]. Recent double electron-electron resonance spectroscopic studies indicate that the redox state of the diiron center strongly effects the conformation of the MMOB N-terminus on the surface of

MMOH. In particular, binding to the reduced protein better orders the flexible N-terminal tail of MMOB, allowing Tyr8 to interact with MMOH and exert its allosteric effects that allow passage of substrate to the cavity at the active site diiron center [144].

A phenomenon commonly observed in the steady state turnover of sMMO is a change in the product distribution when MMOB is added to the reconstituted system [151]. For example, without MMOB the hydroxylation of propane, butane, and nitrobenzene by MMOH yields 61 % 1-propanol, 6 % 1-butanol, and 10 % p-nitrophenol. With MMOB, yields of 93 % 1-propanol, 56 % 1-butanol, and 90 % p-nitrophenol are achieved. The general trend for the many substrates that have been tested with sMMO is that MMOB shifts regiospecificity such that mostly primary alcohols and para-substituted aromatic alcohols are formed. In other words, MMOB changes the morphology of the active site such that the primary carbon on alkanes and the C4 position on mono-substituted aromatics are preferentially presented to the activated oxygen species at the diiron center. Similar changes in regiospecificity are observed in the toluene monooxygenase systems when the regulatory protein is added [152], suggesting the general structural effect is conserved among BMMs. Initial insight into the regulatory protein-dependent regiospecificity changes was provided by the structure of a 6-bromohexanol-soaked MMOH crystal in which an unexpected α- to π-helix transition in MMOH helix E elongated the active site pocket and increased its overall volume [109]. The structures of the MMOH-MMOB, PHH-PHM, and T4MOH-T4MOD complexes later revealed a similar structural change, in addition to new ones that would explain some, but not all, of the observations described above.

3.4.3 Structures of Regulatory Protein-Hydroxylase Complexes

The long sought structure of the MMOH-MMOB complex was solved to 2.9 Å resolution and published in 2013 (Figure 10) [108]. The structure not only confirmed many previously generated ideas about the complex based on the available biochemical information but also revealed intriguing new structural changes that stand in contrast to the structures of related BMM hydroxylase-regulatory protein complexes. The folded MMOB core docks onto MMOH α-subunit helices A, E, and F in the canyon of the $\alpha_2\beta_2$ interface while the long N-terminal tail forms a ring-shaped structure on the α-subunit surface over helices H and 4 (Figure 8). MMOB-induced conformational changes in the hydroxylase are observed primarily in helices E, F, H, and 4. As observed in the 6-bromohexanol-soaked structure of MMOH, residues 212–216 on helix E undergo a small α- to π-helix transition, resulting in conserved Thr213 shifting away from the active site toward the interface between helices E and F (Figure 14). Asn214 moves toward the hydroxylase surface to hydrogen bond with Ser111 of MMOB, and Leu216 slides into the back of the active site cavity 1. The net effect is a lengthening of the substrate binding pocket. Glu209, a ligand to Fe2, is shifted slightly away from its original position in the MMOH structure, but the coordination geometry to the metal center appears unchanged.
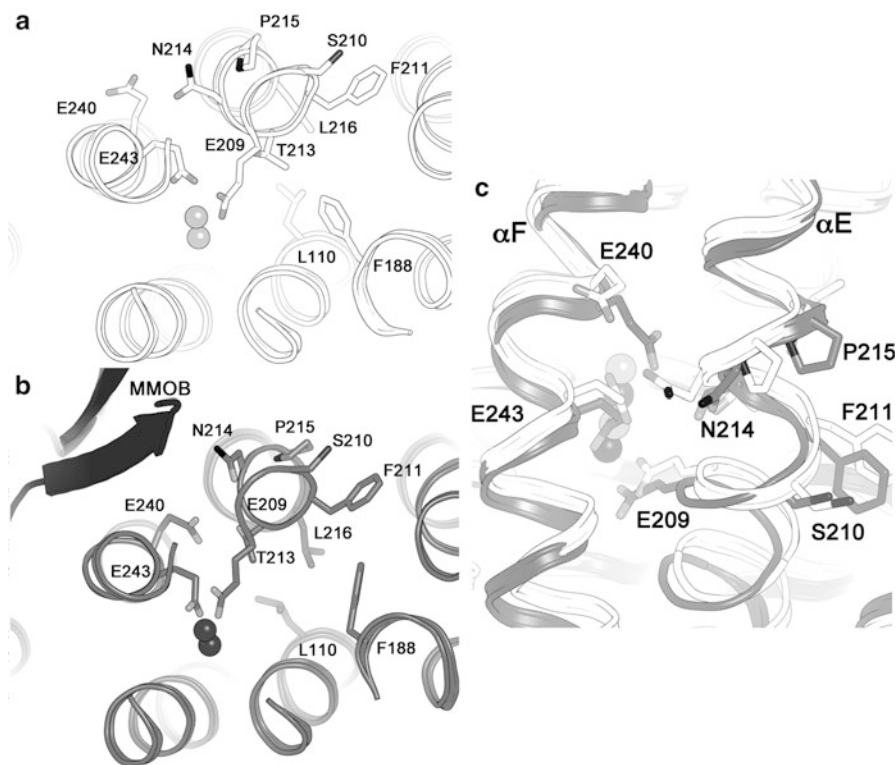
Figure 14 MMOB-induced conformational changes in α-subunit helices E and F. (**a**) MMOH$_{ox}$, (**b**) MMOH-B complex. (**c**) Top down view comparing the helical changes in the MMOH$_{ox}$ (light gray) and MMOH-B (dark gray) structures.

On helix F, residues 240–244 wind more tightly, resulting in the rotation of Glu240 toward the interface between helices E and F (Figure 14). This configuration is stabilized by hydrogen bonding interactions between Glu240 and Thr213 on MMOH and Ser111 on MMOB (Figure 13b). Concomitant with these movements in helices E and F, Glu243 undergoes a carboxylate shift (Figure 15). The positional adjustments in helices H and 4 most likely stem from a repacking of the interface between helices E and F and an optimization of interactions with the MMOB N-terminus. These latter adjustments do not appear to directly influence the active site or the various cavities within the hydroxylase, but may have other, yet undetermined roles. Similar re-arrangements of helices E and F occur in the phenol hydroxylase and toluene 4-monooxygenase systems [103, 104].
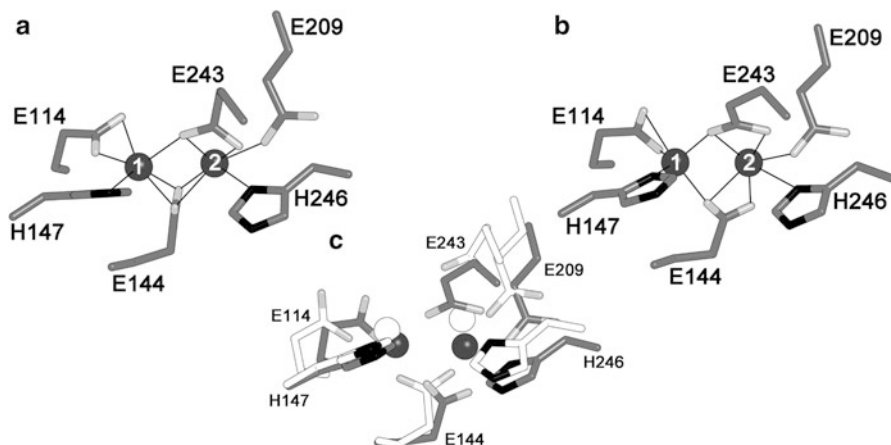
Figure 15 Structure of the MMOH-B diiron active site from two different protomers (**a**, **b**). (**c**) Overlay of the MMOH$_{ox}$ (white) and MMOH-B (gray) diiron centers.

3.4.4 The Activated Soluble Methane Monooxygenase Diiron Center

From the MMOH-MMOB structure, it is clear that the changes in the conformations and positions of helixes E and F propagate toward the diiron center and affect the coordination environment. The "observed" changes, however, must be interpreted with a degree of caution. First, the limited 2.9-Å resolution of the structure does not allow for clear visualization of solvent-derived ligands and will affect the accuracy by which it is possible to model the positions of the amino acid ligands. Second, although the oxidized form of the MMOH-MMOB complex was crystallized, it is conceivable that the X-ray beam led to cryo-reduction of the metal center by one or two electrons to form the mixed-valent or fully reduced state, respectively. As a result, the oxidation state of the diiron center in the MMOH-MMOB structure is uncertain. The metal center has geometric features that are similar to those of both MMOH$_{ox}$ and MMOH$_{red}$ (Figure 15). The carboxylate shift in Glu243 is similar to the one in MMOH$_{red}$ but the average Fe–Fe distance in each of the four metal centers found in the asymmetric unit of the crystal is 3.1 Å, a value closer to the 3.0–3.1 Å distance observed in MMOH$_{ox}$ as opposed to the 3.3–3.4 Å distance in MMOH$_{red}$ and MMOH$_{mv}$ [130].

Although it is a low-resolution structure, some of the iron ligands in the MMOH-MMOB complex seem to adopt new geometries. Glu114 appears to assume a bidentate chelating mode of coordination to Fe1. Glu144 also adjusts its coordination to the iron atoms. In one active site, the side chain rotates by 90° such that the two carboxylate oxygen atoms are orthogonal to the Fe–Fe vector (Figure 15a). In another active site, one oxygen atom bridges both irons and Fe2 is coordinated in a bidentate chelating fashion (Figure 15b). These new configurations for Glu114

and Glu144 may be in response to gross lateral movement of helices E and F that force Glu209, Glu243, His246, and the iron atoms to translate toward the C-terminus of helix F (Figure 15c and 16).
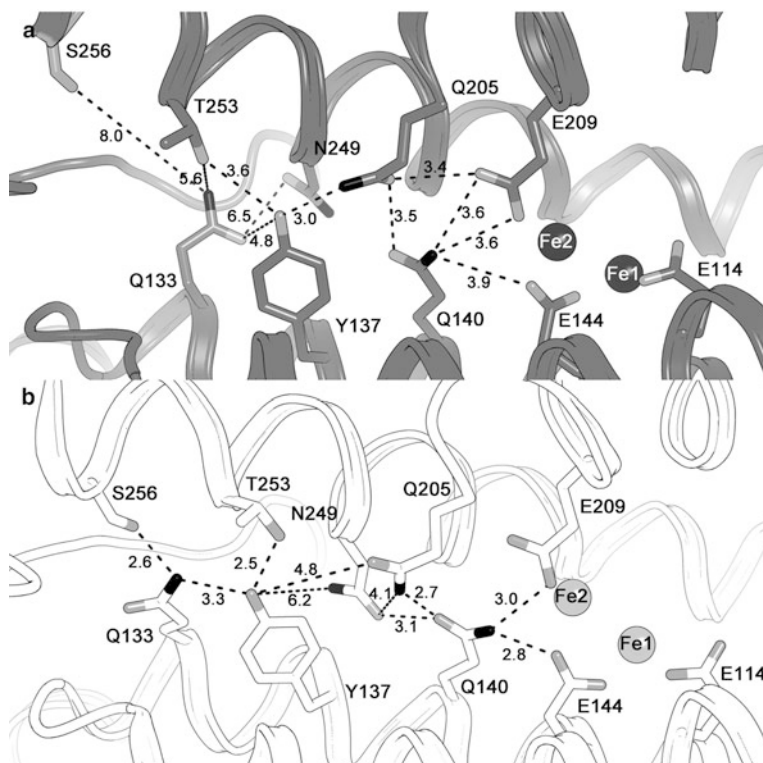
Figure 16 Second and third coordination sphere hydrogen-bonding patterns near Fe2 and Glu209 in (**a**) the MMOH-B complex and in (**b**) MMOH$_{ox}$.

An overlay of the MMOH$_{ox}$ and MMOH-MMOB structures shows the positions of Fe1 and Fe2 to shift by 0.7 Å and 1.3 Å, respectively, to accommodate the helical motions and new positions of some of the amino acid ligands. Because helices B and C do not move much, it is possible that the side-chains of Glu114, Glu144, and His147 on these helices are forced to adjust accordingly to maintain interactions with the iron atoms (Figures 15 and 16). To support this lateral movement along the axis of the four-helix bundle, the hydrogen bonding patterns of the second coordination sphere near Glu209 and Fe2 rearrange. Most notably, Gln140 is no longer in contact with Glu209 and Glu144 (Figure 16).

3.4.5 Comparisons to Toluene Monooxygenases and Phenyl Hydroxylase

One important question in the BMM field is, "Why do the other BMMs not hydroxylate methane?" In the absence of the regulatory protein, the structures of the oxidized and reduced ToMOH and T4MOH diiron centers are nearly identical to those in MMOH [102, 104, 153]. The most glaring difference between sMMO and the TMOs is the occurrence of a long, 30-Å channel in the α-subunit that is required to transport aromatic substrates to the diiron center. This channel contrasts with the cavities in MMOH that follow a similar, but not identical, route through the α-subunit. It is unlikely that the channel affects hydroxylation chemistry, although the greater solvent access in TMOs was a concern because high-valent intermediates could be quenched if the activated metal center were not protected [102].

The global structures of the PHH-PHM and T4MOH-T4MOD complexes are similar to that of MMOH-MMOB with the regulatory protein binding over α-subunit helices A, E, and F in the hydroxylase canyon region. Despite having a much shorter N-terminus, the regulatory protein in these related BMM systems induces nearly identical conformation changes in helices E and F near the diiron center, demonstrating a conserved method for "activating" the hydroxylases. The one surprise from these structures is that the helical changes collapse the substrate channel to create a single pocket near the active site, while simultaneously opening up access to other α-subunit cavities [104]. These cavities were later identified as a major route for O_2 access to the metal center in ToMO [65].

The electron density around the diiron center of the 2.3 Å PHH-PHM structure is difficult to interpret and there are questions about the oxidation state of the metal center and overall occupancy of PHM in the crystal structure. For T4MOH-D, structures of the oxidized and reduced diiron centers look similar to the ones found in $MMOH_{ox}$ and $MMOH_{red}$, (Figures 12 and 17). Although it is difficult to make informative comparisons to the metal center geometry observed in the low resolution structure of the MMOH-B complex at this time, a significant difference between the structures of TMO and sMMO hydroxylase-regulatory protein complexes lies in the second coordination sphere.

Near Fe1 in T4MOH, Glu104 hydrogen bonds with Gln141, which may serve to constrain the position of this iron ligand, as does a water molecule in MMOH (Figure 17) [203]. If Glu114 does in fact alter its configuration in the MMOH-MMOB complex, this difference could be one contributing factor. On the opposite side of the active site near Fe2, the hydrogen bonding patterns are unaltered in the T4MOH and T4MOH-D structures, suggesting a rigid assembly of the T4MOH metal center. By contrast, this network reconfigures in MMOH when the regulatory protein is bound (Figure 16). A relaxing of hydrogen bonding interactions between Gln140 and the coordinating Glu209 and Glu144 ligands possibly affords the sMMO diiron center more conformational freedom. It is tempting to speculate that the additional conformational constraints in other BMM systems prevent them from achieving the high-valent Q intermediate observed sMMO responsible for activating high energy C–H bonds in alkanes.
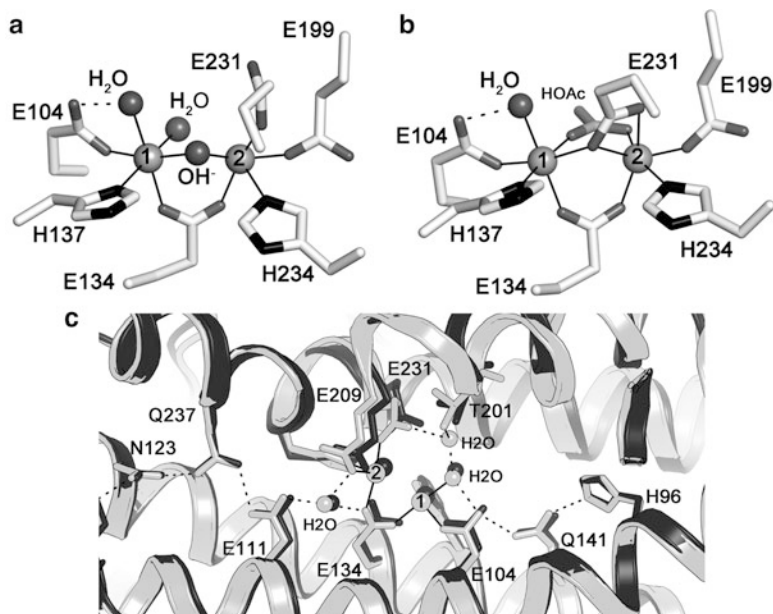
Figure 17 Structures of the (**a**) oxidized (PDB entry 3DHH) and (**b**) reduced (PDB entry 3DHI) T4MOH-D diiron centers. (**c**) Overlay of the second and third coordination sphere hydrogen-bonding patterns near Fe1 and Fe2 in the oxidized T4MOH (dark gray) and the T4MOH-D (light gray) structures.

3.5   Substrate Access to the Catalytic Diiron Center

A challenge for all BMM systems is to deliver substrates to the diiron center with the appropriate timing to support catalysis (Figure 11). The structure of the hydroxylase has suggested defined routes for O_2, hydrocarbon, electrons, and protons to the active site. The timing of delivery of these substrates is critical, not only for maximum catalytic efficiency, but also to avoid unwanted events such as quenching-activated oxygen intermediates. Such quenching leads to the uncoupling of electron consumption from productive utilization of oxygen to convert methane to methanol. Otherwise, MMOH can become an NADH oxidase. In the next section we describe pathways for substrate access and product egress during the catalytic cycle.

3.5.1   Cavities for O_2 and Hydrocarbons

Several hydrophobic cavities have been identified in the MMOH α-subunit, three of which, (cavities 1, 2, and 3) bind xenon, halogenated alkanes, and alcohols of up to eight carbon atoms in length (Figure 8) [109, 110, 154]. The entrance to each cavity is gated by a set of hydrophobic residues that adopt alternate rotamer conformations in MMOH crystal structures with different product alcohols

bound. Cavities 1 and 2 are discontinuous and separated by Leu110 (not shown) and Phe188 (Figure 18a). Cavities 2 and 3 are continuous, but somewhat restricted near Val105, Phe109 and Leu289. The opening and closing of these gates have been proposed as a means for controlling substrate entrance to and/or product egress from the active site pocket (cavity 1) during catalysis [109, 155]. Structures of MMOH$_{red}$ show no changes in cavity structure or positioning of the amino acid gates. Binding of MMOB to the hydroxylase, and subsequent changes in helices E and F, however, force a repositioning of the Leu110 and Phe188 side chains, connecting cavities 1 and 2 such that a pathway extends from the protein surface through the α-subunit to the active site (Figure 18b and 18c). Thus, one of the major functions of MMOB is to facilitate the creation of a freely diffusible space for methane and dioxygen to access the diiron center [108].
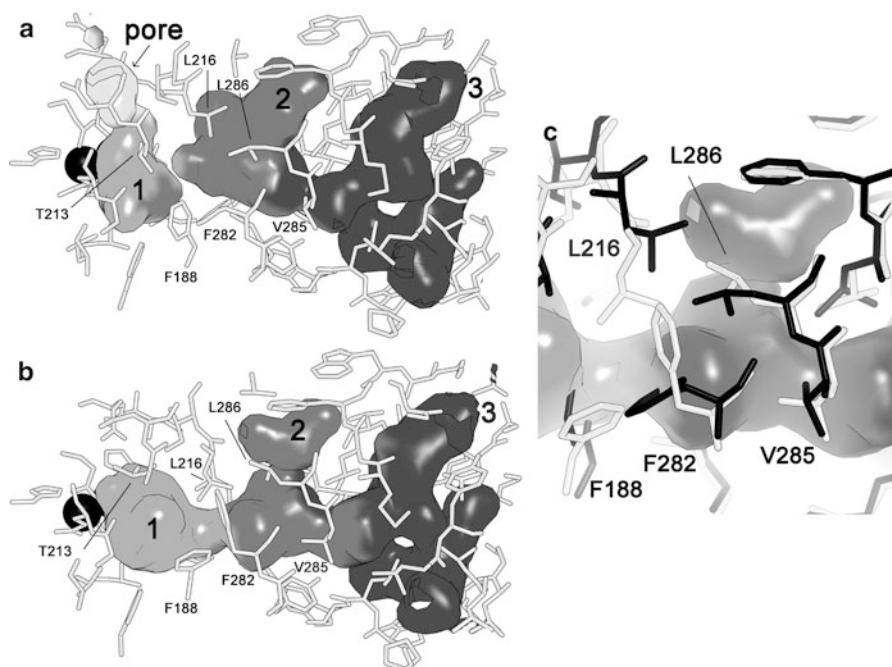
Figure 18 Cavities (1, 2, 3) in the (**a**) MMOH and (**b**) MMOH-B structures. Labeled residues exhibit the largest positional changes. (**c**) Overlay of the MMOH (black) and MMOH-B (light gray) structures depicting positional differences at the interface between the cavities. Cavity surfaces correspond to those in the MMOH-B complex. Val105, Phe109, and Leu289 at the interface between cavities 2 and 3 are not visible in this orientation of the structure. The figure was adapted from [108].

The best evidence that these cavities are functional comes from studies of the TMO system. The structure of the T4MOH-D complex reveals a similar series of cavities through the hydroxylase α-subunit once the regulatory protein binds and

collapses the aromatic substrate channel leading to the active site [104]. Taking advantage of a Thr201Ser mutation in ToMOH that allows observation of the reaction of O_2 with the reduced diiron center, optical stopped-flow spectroscopic investigations of ToMOH variants that restrict or enhance O_2 passage through the cavities revealed that the hydroxylase uses this ~40 Å route as a primary pathway for controlling O_2 diffusion to the iron center [65]. The inability to express sMMOH in a heterologous host has thus far prevented similar experiments being conducted with this enzyme.

In addition to the cavities, a hydrophilic pore formed between MMOH helices E and F involving Asn214, Thr213, and Glu240 was hypothesized to provide the most direct route for the passage of small gaseous substrates or product alcohols to and from the diiron center [109]. Redox dependent shifts in Asn214 rearrange the orientation of amino acid side chains comprising the pore. Because the regulatory protein docks on top of these helices in the different BMM hydroxylase-effector complexes, the pathway leading from the diiron center to the surface through this pore is blocked. Biochemical data showing that MMOB bound to the hydroxylase surface significantly decreases the rate of adventitious iron loss from reduced MMOH, further supports the notion that MMOB can restrict the passage of molecules to and from the diiron center through the pore [92].

Occlusion of the pore by MMOB as well as its hydrophilic character suggest that the pore is unlikely to provide the route of hydrophobic gases to the active site during the catalytic cycle, but dissociation of MMOB could generate a route for hydrophilic methanol and water release at the conclusion of the reaction cycle [108]. The importance of the pore for product release is supported by steady-state and pre-steady state studies of MMOH using an MMOB Asn107Gly/Ser109Ala/Ser110Ala/Thr111A quadruple variant that effectively sculpted the MMOB surface oriented over the hydroxylase diiron center [156]. When monitoring reactions with large substrates like nitrobenzene, this quadruple variant generated a two-fold increase in both steady-state turnover and the rate of product release from the diiron center following oxidation. The rates of methane hydroxylation and product release were unaffected. Work with the quad mutant suggests that product alcohols can escape the enzyme through a pathway at the MMOH-B interface. A major conclusion from all of this work is that the regulatory protein exerts significant control over the movement of compounds into and out of the active site at different stages of the catalytic cycle.

3.5.2 Proton Delivery

The delivery of protons is required for reduction of the dimetallic center and the O_2 activation steps of the sMMO catalytic cycle [157–159]. Solvent is considered the primary source of the protons, but their pathway to the diiron center is largely unknown. The structural changes in MMOH helices E and F near the pore suggest a mechanism for proton delivery whereby movement of Glu240 from the

hydroxylase surface toward the interior initiates opening of the pore and formation of a hydrogen bonding network at the MMOH-MMOB interface using conserved Asn214, Thr213, and Ser111 on MMOB (Figures 13 and 14). Because these residues are unlikely to directly ferry a proton, we propose that water or hydronium ions, such as the one bridging Gln230 (Glu240 in MMOH) and the terminal water coordinated to Fe1 in the T4MOH-D complex, may be important participants in this relay process (Figure 17c).

Unfortunately, little work has been done to investigate the proposed proton transfer pathway except for studies on the role of the conserved threonine in TMOs. Mutagenesis of this residue in T4MOH and ToMOH revealed that substitution of either hydrophobic or hydrophilic residues at this position yields a less active enzyme with efficient coupling but altered substrate regiospecificity [159, 160]. The T4MOH Thr201Ala variant resulted in significant release of hydrogen peroxide from the enzyme following reaction with T4MOHD$_{red}$ with O$_2$, suggesting this threonine may help to stabilize the appropriate iron-bound activated oxygen intermediates [161]. Further study in ToMOH indicated that Thr201 mutants affect the formation and decay kinetics of a peroxodiiron(III) intermediate, and that this residue plays a major role in the proton transfer steps required to generate this species [159, 162]. If the route for proton relay involves Glu240, Asn214, and Thr213, initializing this pathway relay for the controlled delivery of protons through the pore may be one of the primary functions of regulatory proteins in the BMM family.

3.6 Dimetallic Activation of O$_2$ and Methane

Efforts to unravel the sMMO mechanism have focused on how MMOH activates dioxygen, the identity of intermediates that react with hydrocarbons, and how C–H bonds are broken. A detailed understanding of the structures and properties of the different intermediates has been of interest as many laboratories aim to generate synthetic hydrocarbon oxidation catalysts based on a dimetallic iron unit. Mechanistic studies have identified several intermediate species during rapid kinetic experiments, some of which have overlapping properties that are difficult to deconvolute [9]. The fact that more than one intermediate can react with hydrocarbon substrates at one point in time led to confusion about the nature of the C–H bond activation and oxygen insertion process [11]. Among the laboratories [9, 10] focused on establishing a mechanism for the *M. capsulatus* (Bath) *(Mc)* and *M. trichosporium* Ob3b *(Mt)* systems, there is general consensus as to the nature of the major intermediates in the sMMO reaction cycle (Figure 11). Some disagreement still exists as to what their exact structures are and how one might transition to the next. In this section we first discuss single-turnover kinetic studies aimed at identifying the transient oxygen intermediates and their reactivity with substrates, followed by studies focusing on the C–H bond-breaking steps.

3.6.1 Reaction of O₂ with the Reduced Hydroxylase

The transfer of two electrons and two protons to the diiron(III) center of MMOH$_{ox}$ initiates the sMMO catalytic cycle by generating fully reduced MMOH$_{red}$. Its subsequent reaction with O$_2$ is most efficient when two equivalents of MMOB are present, suggesting MMOB-induced conformational changes gate O$_2$ access to the activated metal center [121]. O$_2$-promoted decay of MMOH$_{red}$, which has been monitored at 4 °C in *M. capsulatus* (Bath) by RFQ Mössbauer and in *M. trichosporium* OB3b by EPR spectroscopy, was measured to be 24 s^{-1} at pH 7.0 and 22 s^{-1} at pH 7.7, respectively [141, 163]. The intermediate that forms from the decay of MMOH$_{red}$ is P* (vide infra), but the absence of any observed pH or O$_2$ concentration dependence for the decay of *Mt* MMOH$_{red}$ suggested that a rapid irreversible O$_2$ binding event occurs before P* in which O$_2$ is bound to the hydroxylase but not to the diiron center. This intermediate, termed O, alternatively was interpreted to represent a tight but reversible O$_2$ Michaelis complex to MMOH$_{red}$. However, steady state experiments on *Mc* MMOH using an oxygen electrode failed to provide any evidence for such a complex [164].

3.6.2 Peroxo Intermediates

After reaction with O$_2$, peroxodiiron(III) intermediates are formed. Mössbauer data at 4 K on rapid freeze-quenched samples of MMOH$_{red}$ mixed with O$_2$ reveal a quadrupole doublet with $\delta = 0.66$ mm s^{-1} and $\Delta E_Q = 1.51$ mm s^{-1} [165, 166]. These parameters are indicative of an antiferromagnetically coupled, high-spin diiron(III) center in which each Fe^{III} ion has a similar coordination geometry. UV-vis stopped-flow spectroscopy revealed optical features at 420 nm and 720 nm in *Mc* MMOH and 700 nm in *Mt* MMOH [141, 166, 167]. Although the decay constants of this intermediate measured by RFQ Mössbauer and stopped-flow UV-vis spectroscopy were similar in *Mc* MMOH (~0.36 s^{-1} at 4 °C), the measured rate constants obtained by these methods for the formation of the peroxo intermediate were significantly different, namely, ~1 s^{-1} by stopped-flow and ~25 s^{-1} by Mössbauer [167]. This discrepancy suggested the existence of two peroxodiiron(III) species, P* and H$_{peroxo}$, having similar Mössbauer properties but different, overlapping optical signals. A re-examination of the intermediates in *Mt* MMOH by stopped-flow UV-vis spectroscopy required an additional intermediate preceding H$_{peroxo}$ to fit the data. This intermediate, P*, which was presumed to have no optical features at 420 nm, formed with a rate constant of 22–26 s^{-1} at 4 °C followed by H$_{peroxo}$ at ~9–12 s^{-1} [168, 169]. This rate was consistent with earlier observations, establishing P* as the first intermediate resulting from MMOH$_{red}$ reacting with O$_2$. More recently, in a MMOB His33Ala variant in *Mt* MMOH, the conversion of P* to P was retarded, facilitating the trapping of larger quantities for characterization [168]. This intermediate had Mössbauer parameters indicative of a diiron(II) center, no significant optical features, and no $g = 16$ EPR signal that is characteristic of the

diiron(II) center in MMOH$_{red}$. In contrast, subsequent UV-vis stopped flow studies of *Mc* MMOH in the presence of methane, to eliminate underlying optical signals of intermediate Q, suggest that P* is an optically active diiron(III) center with absorption maxima at 420 nm ($\varepsilon = 3500\,M^{-1}\,cm^{-1}$) and 720 nm ($\varepsilon = 1250\,M^{-1}\,cm^{-1}$) that overlap with the ensuing H$_{peroxo}$ and Q intermediates [205]. It is unclear, based on the latter two investigations, whether or not P* in *Mc* MMOH is the same intermediate as that observed in *Mt* MMOH.

Table 2 Spectroscopic Parameters of Peroxodiiron(III) Intermediates.

	Optical		Mössbauer		
	λ_{max} (nm)	ε ($M^{-1}\,cm^{-1}$)	δ (mm s^{-1})	ΔE_Q (mm s^{-1})	Peroxide Binding Mode
MMOH H$_{peroxo}$ (*Mc*)	420; 720	3880; 1350[a]	0.66	1.51[b]	
MMOH H$_{peroxo}$ (*Mt*)	725	2500[c]	0.67	1.51[d]	
MMOH P* (*Mc*)	420; 720	3500; 1250[a]			
ToMOH$_{peroxo}$			0.54	0.67[e]	
ToMOH Thr201Ser$_{peroxo}$	675	1500[f]	0.67	1.51[f]	
RNR-R2 Asp84Glu	700	1500[g]	0.63	1.58[g]	μ-1,2[h]
Δ9-desaturase	700	1200[i]	0.68; 0.64	1.90; 1.06[i]	μ-1,2[j]
Frog M ferritin	650[k]		0.62	1.08[k]	μ-1,2[l]
hDOHH[m]	630	2800	0.55; 0.58	1.16; 0.88	μ-1,2
[Fe$_2$(μ-1,2-O$_2$)-(μ-O$_2$CCH$_2$Ph)$_2$-{HB(pz')$_3$}$_2$][n]	694	2650	0.66	1.40	gauche μ-1,2
[Fe$_2$(μ-OH)(μ-1,2-O$_2$)-(6-Me$_2$-BPP)$_2$]$^+$[o]	644	3000	0.50	1.31	*cis*-μ-1,2
[Fe$_2$(μ-O)(μ-1,2-O$_2$)-(6-Me$_3$-TPA)$_2$]$^{2+}$[p]	494; 648	1100;1200	0.54	1.68	*cis*-μ-1,2

[a][157]
[b][141]
[c][158]
[d][166]
[e][173]
[f][162]
[g][190], RNR-R2 = ribonucleotide reductase R2 subunit, Asp84Glu mutation.
[h][191]
[i][192]
[j][193]
[k][194]
[l][195]
[m][196], hDOHH = human deoxyhypusine hydroxylase.
[n][197], pz' = 3,5-bis(isopropyl)-pyrazolyl.
[o][198], BPP = *N,N*-bis(2-pyridylmethyl)-3-aminopropionate.
[p][199], TPA = tris(2-pyridylmethyl)amine.

Assuming P* to be a diiron(III) complex, the observation of optical bands is key, for it allows for more informed comparisons to peroxodiiron(III) species in well characterized model complexes and enzymes (Table 2). Based on similarities in their optical and Mössbauer properties, P* and H_{peroxo} are expected to have a μ-1,2-peroxo diiron(III) core but probably differ in the configuration of surrounding ligands. Possible peroxo structures are presented in Figure 19a and take into consideration the different binding modes of Glu-243 (1–8). The gauche μ-1,2 configuration of the $[Fe_2(\mu$-1,2-$O_2)(\mu$-$O_2CCH_2Ph)_2\{HB(pz')_3\}_2]$ model complex is the most interesting model because its Mössbauer parameters are nearly identical to those of P* (3 or 4) [170]. Computational work also seems to favor this binding mode as opposed to cis-μ-1,2 and μ- η^2:η^2 geometries (1, 2, and 7) [171, 172]. Interestingly, the optical and Mössbauer properties of the ToMOH peroxo intermediate are quite different from those of the MMOH peroxo intermediate, suggesting that the structure of the ToMOH peroxo species (possibly 5 or 6) is the point of departure in their mechanisms [172–174].
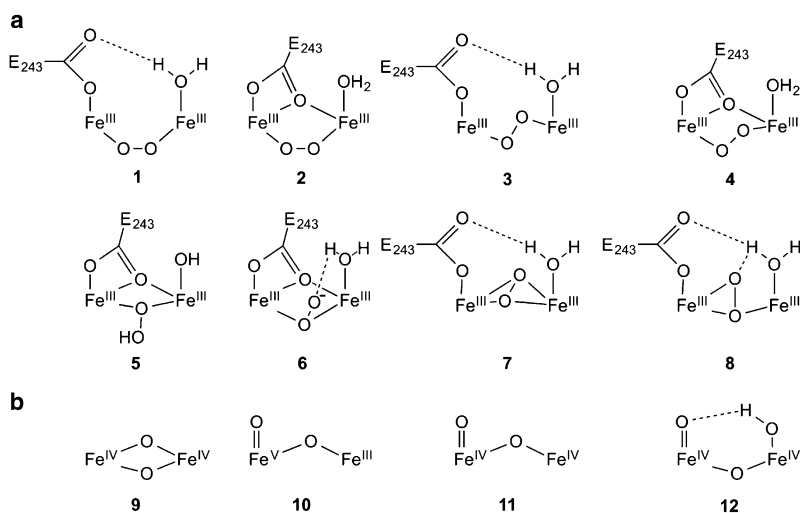
Figure 19 (**a**) Proposed structures of peroxodiiron(III) intermediates. (**b**) Possible structures for intermediate Q. The figure was adapted from [9].

The conversion of P* to H_{peroxo} is pH-dependent and has a kinetic solvent isotope effect (KSIE) in D_2O of $k_H/k_D=2.0$ for *Mc* MMOH and $k_H/k_D=1.3$ for *Mt* MMOH [157, 158]. Fits to the data from both enzyme systems are consistent with the kinetic model 1 in Figure 20. Given the similar spectroscopic parameters of these intermediates, the major structural difference between P* and H_{peroxo} is probably a proton transfer event that does not significantly perturb the diiron(III)-oxygen core (Figure 11). Because the spectroscopic properties of peroxo- and

hydroperoxo-diiron(III) species are expected to be significantly different [175], Glu243 was proposed to be the recipient of this proton [9]. Further work is required to confirm the structures of the P* and H_{peroxo} intermediates, which are important unsolved questions.

Model 1: $P* + H^+ \underset{K_a}{\rightleftharpoons} [P*-H] \xrightarrow{k_{HA}} [H_{peroxo}]$

Model 2: $H_{peroxo} + H^+ \underset{K_a}{\rightleftharpoons} [H_{peroxo}-H] \xrightarrow{k_{HA}} Q$

Model 3: $H_{peroxo} + H^+ \underset{K_1}{\rightleftharpoons} [H_{peroxo}-H] + H^+ \underset{K_2}{\rightleftharpoons} [H_{peroxo}-H] \xrightarrow{k_{H2A}} Q$

$\downarrow k_{HA}$

Q

Figure 20 Kinetic models for the sMMO proton transfer steps. The figure was adapted from [9].

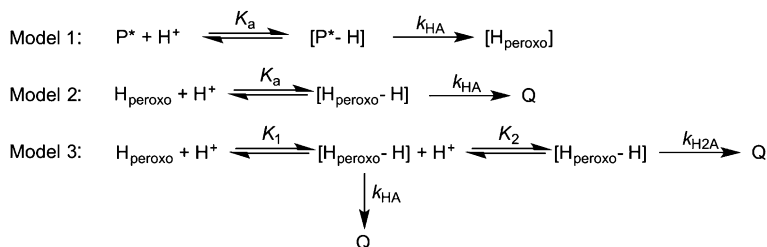### 3.6.3 Intermediates Q and Q*

Electron-rich substrates, like propylene and diethylether, react with H_{peroxo} to form oxidized products and $MMOH_{ox}$ via a two-electron transfer mechanism [167, 176, 177] (Figure 11). In the absence of such substrates, homolytic cleavage of the H_{peroxo} O–O bond leads to formation of intermediate Q, the species responsible for activating the C–H bond in methane. Q is an antiferromagnetically coupled diiron(IV) intermediate with a bright yellow color and absorption maxima at 330 nm and 420 nm (Table 3) [141, 163, 165, 178]. The measured rate constants for Q formation, 0.36 s^{-1} and 2.5 s^{-1} at 4 °C in *Mc* and *Mt* MMOH, respectively, coincide with the rate of H_{peroxo} decay [157, 169]. Mössbauer spectral studies of Q from *Mt* MMOH show a single quadrupole doublet, indicating that both Fe(IV) atoms have similar ligand environments [178]. This information, coupled with an XAS spectrum of *Mt* Q fit with a short Fe–Fe distance of 2.46 Å and Fe–O/N bond lengths of 1.77 Å and 2.05 Å, lead to the interpretation of Q as being a di(μ-oxo)diiron(IV) species (Figure 19b, **9**) [166].

In the presence of methane, Q converts to $MMOH_{prod}$ (or $MMOH_{ox}$) with rate constants of 3.9 s^{-1} and 2.9 s^{-1} at 4 °C for *Mc* and *Mt* MMOH, respectively [128, 157, 169]. In the absence of substrates, Q decays to $MMOH_{ox}$ by acquiring two electrons and two protons by a relatively uncharacterized process. An intermediate in this decay pathway, Q*, was identified by UV-vis stopped-flow spectroscopy to have an absorption maximum at 420 nm, like Q, but a unique shoulder at 455 nm that is unaffected by substrate concentration [157]. The formation and decay rates for Q* were measured at 4 °C in *M. capsulatus* (Bath) MMOH to be 0.01 s^{-1} and 0.0028 s^{-1}, respectively. The reason for the formation of such an intermediate is unclear, but, the collapse of Q to a non-reactive thermodynamically

Table 3 Spectroscopic Parameters of Intermediate Q and High-Valent Non-heme Diiron Complexes.

	Optical		Mössbauer		
	λ_{max} (nm)	ε (M^{-1} cm^{-1})	δ (mm s^{-1})	ΔE_Q (mm s^{-1})	Fe–Fe (Å)
MMOH Q (*Mc*)	420	8415[a]	0.21; 0.14	0.68; 0.55[b]	
MMOH Q (*Mt*)	330; 420	7500; 7500[c]	0.17	0.53[d]	2.46[e]
MMOH Q* (*Mc*)[f]	420 (455 shoulder)				
$[Fe_2(\mu\text{-}O)_2(L)_2]^{3+}$	366; 616	7900; 5200[g]	0.48; 0.08	1.6; 0.5[h]	2.68[i]
$[Fe_2(\mu\text{-}O)_2(L)_2]^{4+j}$	485; 875	9800; 2200	−0.04	2.09	2.73

[a][157]
[b][141]
[c][163]
[d][178]
[e][166]
[f][157]
[g][200], L = 5-Me$_3$-TPA; TPA = tris(2-pyridylmethyl)amine.
[h][201], L = 6-Me$_3$-TPA.
[i][202], L = 5-Et$_3$-TPA.
[j][183], L = tris((4-methoxy-3,5-dimethylpyrid-2-yl)d$_2$-methyl)amine.

more stable intermediate such as Q* in the absence of substrate may protect the active site from radical initiated damage by the more reactive Q species.

The conversion H_{peroxo} to Q is pH-dependent and exhibits KSIEs of $k_H/k_D = 1.8$ for *Mc* MMOH and $k_H/k_D = 1.4$ for *Mt* MMOH, making Q formation a proton-dependent step [157, 158]. Q to Q* conversion, on the other hand, is pH-independent. Kinetic data for the pH dependent conversion of H_{peroxo} to Q are best fit in *Mt* MMOH by using single ionizing system and a pK_a of 7.6 (Figure 20, kinetic model 2). For this same step, *Mc* MMOH requires a doubly ionizing system with pK_a values of 7.8 and 7.2, suggesting a second proton transfer event during this transformation (Figure 20, kinetic model 3). Accounting for all the available kinetic data, proton-assisted heterolytic cleavage of the O–O bond best describes the possible series of transitions from P* to Q in *Mc* sMMO (Figure 11) [9, 157].

The discovery of Q* has added to a growing list of evidence suggesting the structure of Q needs further evaluation. Unlike the Mössbauer spectrum of *Mt* Q in which one quadrupole doublet was observed, early analysis of *Mc* Q samples showed two quadrupole doublets of equal intensity [141, 165], suggesting the presence of a second similar species that may be Q*. The long lifetime of Q* is a concern with regard to the preparation of samples for RFQ Mössbauer and XAS. For example, in the 186 seconds age time of the optical stopped flow experiments performed in the absence of substrate to examine the kinetics of the different Q intermediates, it was estimated that 19 % and 60 % of the species present were Q and Q*, respectively [157]. It is conceivable that fits to XAS data on *Mt* MMOH

modeled Q* or an average of the two diiron(IV) intermediates as opposed to Q alone. Adding to the concern, many DFT calculations fail to reproduce the short Fe–Fe distance observed by XAS [179, 180]. To generate this intermediate, protein scaffold may compress the iron atoms in order to achieve favorable energetic conversion from H_{peroxo} to Q, as suggested by QM/MM studies [180].

Several synthetic catalysts that achieve a high-valent diiron species capable of oxygen insertion between C–H bonds offer some insight into alternative possibilities for the structure of Q, in which the oxidizing potency of the complex is concentrated at a single $Fe^{IV}=O$ unit (Figure 20). As an example, a $[Fe_2(H_2Hbamb)_2(N\text{-melm})_2]$ complex oxidized cyclohexane to cyclohexanol via an $Fe^{II}Fe^{IV}$ intermediate with a terminal $Fe^{IV}=O$ species [181]. An analogous $Fe^{III}Fe^{V}$ center was suggested for Q in MMOH (**10**). A valence-delocalized $[OH\text{–}Fe^{III}\text{–}O\text{–}Fe^{IV}=O]^{2+}$ unit complexed to tris((4-methoxy-3,5-dimethyl-pyrid-2-yl)d$_2$-methyl)amine oxidized C–H bonds a million times faster than a valence-delocalized "diamond core" analogue, $[Fe^{3.5}(\mu\text{-O})_2Fe^{3.5}]^{3+}$ [182]. In one instance, oxidation by a complex with a $[Fe^{IV}(\mu\text{-O})_2Fe^{IV}L^2]^{4+}$ core was 100 times slower than the corresponding mononuclear Fe(IV)=O complex using the same ligand [183]. These findings suggest that a terminal Fe=O unit (**11** and **12**) may be more effective than a di(μ-oxo)diiron(IV) unit for C–H bond activation.

3.6.4 The Product-Bound Hydroxylase

The oxidation of substrates by Q leads to the product-bound state, $MMOH_{prod}$. This intermediate has only been kinetically observed for oxidation of nitrobenzene to *p*-nitrophenol. Here, product release from the hydrophobic active site promotes formation of the optically detectable *p*-nitrophenolate ion in solution [141, 163]. For this substrate, the rate of steady-state turnover is similar to the rate of product release, indicating product release to be the rate-limiting step in the reaction, at least when nitrobenzene is the substrate. Product displacement may be accomplished either by ligand exchange with solvent or by reduction of the metal center to reinitiate the catalytic cycle. Further studies of product release with other substrates more similar to methane would be valuable.

X-ray structures of $MMOH_{ox}$ crystals soaked with halogenated and non-halogenated alcohols of 1–6 carbons in length reveal that these molecules can readily displace a hydroxide ion and bind to the bridging position between the iron atoms, leaving the surrounding ligand environment unperturbed [109, 154]. The product-bound structures are consistent with EPR, ENDOR, UV-vis, and resonance Raman spectroscopic characterization of $MMOH_{prod}$ in the absence of MMOB [148, 184, 185]. The addition of MMOB influences exogenous ligand binding to the diiron center, as indicated by EPR [148]. It is conceivable that the structure of the diiron center in the MMOH-MMOB product complex is different from the one observed in MMOH alone.

3.6.5   C–H Bond Activation by Different Intermediates

Like the O_2-activation steps, C–H bond activation by sMMO has also received significant attention to determine the mechanism by which the different intermediates activate hydrocarbons. Mechanistic chiral alkane and radical clock substrate probes that rearrange to specific products when a particular hydrocarbon intermediate is generated have been employed to qualitatively differentiate between radical, cationic, and concerted mechanisms (Figure 6). The results of these experiments were not straightforward and have been the subject of considerable debate, reviewed thoroughly elsewhere [11]. Computational methods have added additional insight and, in some cases, explain some of the more paradoxical results.

Small chiral alkanes that closely mimic the natural sMMO substrate were used as reporters for the H-atom abstraction mechanism by intermediate Q [186, 187]. In principle, a concerted mechanism would produce complete retention or inversion of stereochemistry whereas radical and cationic intermediates would predict full racemization (Figure 7). For *M. capsulatus* (Bath) and *M. trichosporium* OB3b sMMO, hydroxylation of (S) or (R)-[1-$^3H_1$,$^2H_1$] ethane yielded a 70:30 retention: inversion of configuration ratio. Reactions with [2-^3H] butane exhibited ~90 % retention. These results could be interpreted as evidence for a radical intermediate, but to achieve 70 % retention of configuration requires the ethyl radical to recombine with the iron-bound hydroxyl radical at a rebound rate of 1×10^{13} s^{-1} [188]. This large value excludes the possibility of a discrete radical intermediate, which would racemize in less than 1×10^{-10} s. DFT calculations provided some clarity to this discrepancy, demonstrating that sMMO may have a "bound-radical" intermediate with restricted rotation owing to weak interactions with the diiron center [189].

Radical clock substrate probes offered an additional way to probe the C–H activation process. For these substrates, H-atom or hydride abstraction by sMMO leads to a radical or cationic intermediate on a constrained hydrocarbon substrate that subsequently rearranges to produce a lower energy, less constrained product alcohol. An example of this rearrangement is shown in Figure 21. Some probes detect only radical products, whereas others, in theory, elegantly differentiate between either a cationic or radical rearrangement [11].

Because the rate constant for the rearrangement of these substrates is known, it is possible to estimate the lifetimes of transient species. Analysis of the reactions with the various probes shows the predominant products to be unrearranged hydroxylated compounds. The minor products, however, were derived from *both* radical and cationic intermediates. These contradictory findings, while perplexing, suggested that sMMO utilizes more than one oxidizing species to activate C–H bonds. Stopped-flow spectroscopic experiments monitoring the reaction of H$_{peroxo}$ with propylene provided the first direct evidence that this Q precursor is reactive toward electron-rich substrates [167]. Further investigation of H$_{peroxo}$ reactions with ethers demonstrated that this intermediate reacts with more electron-rich substrates faster than Q, via a two-electron transfer mechanism as opposed to single-electron transfer steps by Q [176] (Figure 22).
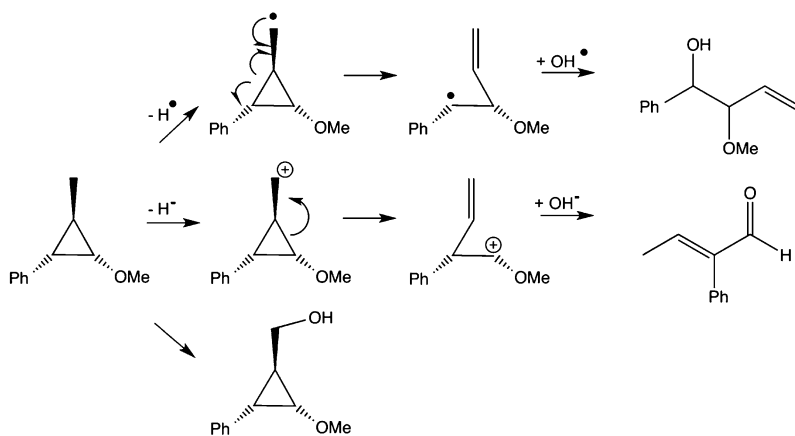
Figure 21 Example of a radical clock substrate (*trans,trans*-2-methoxy-3-phenylcyclopropyl)-methane used on sMMO, that can differentiate between radical and cationic based hydroxylation. The figure was adapted from [8].
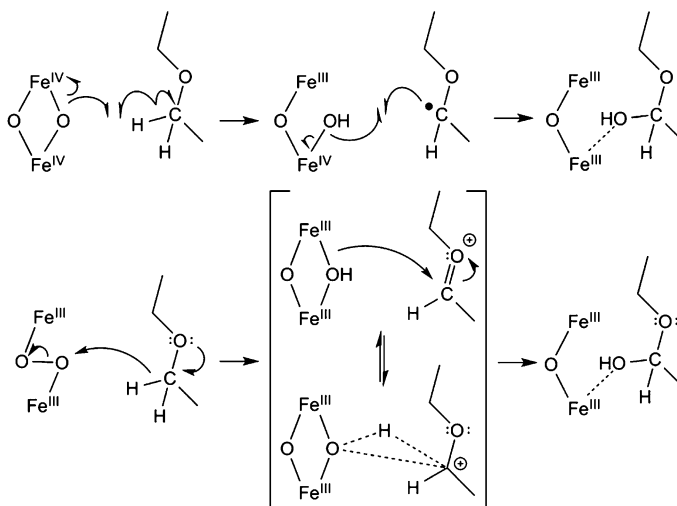

Figure 22 Proposed mechanism of C–H bond activation of diethylether by intermediate Q (**top**) and H$_{peroxo}$ (**bottom**). The figure was adapted from [176].

A concern stemming from the work with radical clock substrates was the low percentage of re-rearranged radical clock-derived products [11]. If Q were to react with hydrocarbons via a traditional radical-based mechanism, a higher yield of radical-derived products was expected. Like the chiral alkane results, DFT calculations suggest the low yields of radical-derived products are explained by a mechanism using "bound radical" with restricted rotation (Figure 6) [189]. Calculations examining a concerted mechanism indicated this pathway to be less favorable.

4   Concluding Remarks and Future Directions

In the last twenty-five years, investigations of the pMMO and sMMO systems, including the organisms that utilize these enzymes, have considerably improved our understanding of the biological transformation of methane to methanol at dinuclear copper and iron centers. As the general picture of the O_2 and C–H activation processes becomes clear, attention now turns toward pursuing a more detailed mechanistic understanding of the hydroxylation chemistry. In particular, it is important to identify the structures of the activated dioxygen intermediates and to sort out the intricacies of the electron and proton transfer events critical for the conversion of one intermediate to the next for methane oxidation.

The controlled delivery of the requisite protons, electrons, oxygen, and hydrocarbon substrates at the appropriate time in the catalytic cycle is essential for efficient hydroxylation chemistry. Failure to regulate when the different substrates arrive at the active site would lead to uncoupling, quenching the activated oxygen intermediates and forming hydrogen peroxide and/or water.

How sMMO controls the timing and assembly of substrates at its diiron center is now reasonably well understood, but this information is lacking for the pMMO system. With sMMO, having multiple protein components has made the process challenging, and information about the electron transfer steps from MMOR to MMOH is incomplete. Although we are much closer to understanding the intricacies of these enzymes, how the sMMO and pMMO protein scaffolds and metal centers work in concert remains a continuing goal as we try to reveal how biology masterfully tunes the reactivity of these unique dinuclear metal centers to carry out their challenging hydroxylation chemistry.

Abbreviations and Definitions

AMO   ammonia monooxygenase
BMMs   bacterial multicomponent monooxygenases
CD   circular dichroism
DFT   density functional theory

EM	electron microscopy
ENDOR	electron nuclear double resonance spectroscopy
EPR	electron paramagnetic resonance spectroscopy
FAD	flavin adenine dinucleotide
Fd	ferredoxin
H$_4$HBamb	2,3-bis(2-hydroxybenzamido)-dimethylbutane
H$_{peroxo}$	sMMO peroxo intermediate
KSIE	kinetic solvent isotope effect
Mc	*Methylococcus capsulatus* (Bath)
MCD	magnetic circular dichroism spectroscopy
melm	*N*-methylimizadole
Mt	*Methylosinus trichosporium* OB3b
MDH	methanol dehydrogenase
MMO	methane monooxygenase
MMOB	soluble methane monoxygenase regulatory protein
MMOD	soluble methane monoxygenase component D
MMOH	soluble methane monoxygenase hydroxylase
MMOH$_{ox}$	oxidized soluble methane monoxygenase hydroxylase
MMOH$_{prod}$	product bound soluble methane monoxygenase hydroxylase
MMOH$_{red}$	reduced soluble methane monoxygenase hydroxylase
MMOH-B	soluble methane monoxygenase hydroxylase-regulatory protein complex
MMOG	soluble methane monoxygenase GroEL-like chaperone
MMOR	soluble methane monoxygenase reductase
NADH	nicotinamide adenine dinucleotide (reduced)
P*	sMMO peroxo intermediate
PH	phenol hydroxylase
PHH	hydroxylase component of phenol hydroxylase
PHM	regulatory protein component of phenol hydroxylase
PHH-M	phenol hydroxylase regulatory protein complex
pMMO	particulate methane monooxygenase
pmoA	26-kDa subunit of pMMO
pmoB	45-kDa subunit of pMMO
pmoC	23-kDa subunit of pMMO
pz'	3,5-bis(isopropyl)-pyrazolyl
Q	sMMO intermediate
Q*	sMMO intermediate (activated)
QM/MM	quantum mechanics/molecular mechanics
sMMO	soluble methane monooxygenase
spmoB	soluble domains of the pmoB subunit
spmoBD1	soluble domain 1 of the pmoB subunit
spmoBD2	soluble domain 2 of the pmoB subunit
T4MO	toluene 4-monooxygenase
T4MOD	toluene 4-monooxygenase regulatory protein

T4MOH	toluene 4-monooxygenase hydroxylase
T4MOH-D	toluene 4-monooxygenase hydroxylase-regulatory protein complex
THFMO	tetrahydrofuran monooxygenase
TMO	toluene monooxygenase family
ToMO	toluene/o-xylene monoxygenase
ToMOD	toluene/o-xylene monooxygenase regulatory component
ToMOH	toluene/o-xylene monooxygenase hydroxylase component
ToMOH-D	toluene/o-xylene monooxygenase hydroxylase-regulatory protein complex
TPA	tris(2-pyridylmethyl)amine
XAS	X-ray absorption spectroscopy
ZSM-5	zeolite socony mobil-5

References

1. US Environmental Protection Agency, in "Methane and Nitrous Oxide Emissions From Natural Sources", Ed US Environmental Protection Agency, Washington DC, USA, 2010.
2. R. S. Hanson, T. E. Hanson, *Microbiol. Rev.* **1996**, *60*, 439–471.
3. H. Jiang, Y. Chen, P. X. Jiang, C. Zhang, T. J. Smith, J. C. Murrell, X. H. Xing, *Biochem. Eng. J.* **2010**, *49*, 277–288.
4. R. Balasubramanian, A. C. Rosenzweig, *Acc. Chem. Res.* **2007**, *40*, 573–580.
5. M. A. Culpepper, A. C. Rosenzweig, *Crit. Rev. Biochem. Mol.* **2012**, *47*, 483–492.
6. A. S. Hakemian, A. C. Rosenzweig, *Annu. Rev. Biochem.* **2007**, *76*, 223–241.
7. R. L. Lieberman, A. C. Rosenzweig, *Crit. Rev. Biochem. Mol.* **2004**, *39*, 147–164.
8. M. Merkx, D. A. Kopp, M. H. Sazinsky, J. L. Blazyk, J. Müller, S. J. Lippard, *Angew. Chem. Int. Edit.* **2001**, *40*, 2782–2807.
9. C. E. Tinberg, S. J. Lippard, *Acc. Chem. Res.* **2011**, *44*, 280–288.
10. B. J. Wallar, J. D. Lipscomb, *Chem. Rev.* **1996**, *96*, 2625–2657.
11. M.-H. Baik, M. Newcomb, R. A. Friesner, S. J. Lippard, *Chem. Rev.* **2003**, *103*, 2385–2419.
12. J. D. Semrau, A. A. DiSpirito, S. Yoon, *FEMS Microbiol. Rev.* **2010**, *34*, 496–531.
13. H. Ali, J. C. Murrell, *Microbiology* **2009**, *155*, 761–771.
14. D. W. Choi, R. C. Kunz, E. S. Boyd, J. D. Semrau, W. E. Antholine, J. I. Han, J. A. Zahn, J. M. Boyd, A. M. de la Mora, A. A. DiSpirito, *J. Bacteriol.* **2003**, *185*, 5755–5764.
15. S. H. Stanley, S. D. Prior, D. J. Leak, H. Dalton, *Biotechnol. Lett.* **1983**, *5*, 487–492.
16. S. D. Prior, H. Dalton, *J. Gen. Microbiol.* **1985**, *131*, 155–163.
17. R. Balasubramanian, A. C. Rosenzweig, *Curr. Opin. Chem. Biol.* **2008**, *12*, 245–249.
18. M. W. Fitch, D. W. Graham, R. G. Arnold, S. K. Agarwal, P. Phelps, G. E. Speitel, G. Georgiou, *Appl. Environ. Microbiol.* **1993**, *59*, 2771–2776.
19. A. A. DiSpirito, J. A. Zahn, D. W. Graham, H. J. Kim, C. K. Larive, T. S. Derrick, C. D. Cox, A. Taylor, *J. Bacteriol.* **1998**, *180*, 3606–3613.
20. C. M. Tellez, K. P. Gaus, D. W. Graham, R. G. Arnold, R. Z. Guzman, *Appl. Environ. Microbiol.* **1998**, *64*, 1115–1122.
21. J. Colby, D. I. Stirling, H. Dalton, *Biochem. J.* **1977**, *165*, 395–402.

22. I. J. Higgins, D. J. Best, R. C. Hammond, *Nature* **1980**, *286*, 561–564.

23. J. Green, H. Dalton, *J. Biol. Chem.* **1989**, *264*, 17698–17703.

24. B. G. Fox, J. G. Borneman, L. P. Wackett, J. D. Lipscomb, *Biochemistry* **1990**, *29*, 6419–6427.

25. K. K. Andersson, W. A. Froland, S. K. Lee, J. D. Lipscomb, *New J. Chem.* **1991**, *15*, 411–415.

26. M. J. Rataj, J. E. Kauth, M. I. Donnelly, *J. Biol. Chem.* **1991**, *266*, 18684–18690.

27. S. I. Chan, K. H. C. Chen, S. S. F. Yu, C. L. Chen, S. S. J. Kuo, *Biochemistry* **2004**, *43*, 4421–4430.

28. K. Burrows, A. Cornish, D. Scott, I. J. Higgins, *J. Gen. Microbiol.* **1984**, *130*, 327–333.

29. D. D. Smith, H. Dalton, *Eur. J. Biochem.* **1989**, *182*, 667–671.

30. R. L. Lieberman, A. C. Rosenzweig, *Nature* **2005**, *434*, 177–182.

31. S. Stolyar, A. M. Costello, T. L. Peeples, M. E. Lidstrom, *Microbiology* **1999**, *145*, 1235–1244.

32. D. J. Arp, L. A. Sayavedra-Soto, N. G. Hommes, *Arch. Microbiol.* **2002**, *178*, 250–255.

33. P. Basu, B. Katterle, K. K. Andersson, H. Dalton, *Biochem. J.* **2003**, *369*, 417–427.

34. R. L. Lieberman, D. B. Shrestha, P. E. Doan, B. M. Hoffman, T. L. Stemmler, A. C. Rosenzweig, *Proc. Natl. Acad. Sci. USA* **2003**, *100*, 3820–3825.

35. H. H. T. Nguyen, S. J. Elliott, J. H. K. Yip, S. I. Chan, *J. Biol. Chem.* **1998**, *273*, 7957–7966.

36. S. S. F. Yu, K. H. C. Chen, M. Y. H. Tseng, Y. S. Wang, C. F. Tseng, Y. J. Chen, D. S. Huang, S. I. Chan, *J. Bacteriol.* **2003**, *185*, 5915–5924.

37. A. Miyaji, T. Kamachi, I. Okura, *Biotechnol. Lett.* **2002**, *24*, 1883–1887.

38. J. A. Zahn, A. A. DiSpirito, *J. Bacteriol.* **1996**, *178*, 1018–1029.

39. S. M. Smith, S. Rawat, J. Telser, B. M. Hoffman, T. L. Stemmler, A. C. Rosenzweig, *Biochemistry* **2011**, *50*, 10231–10240.

40. R. L. Lieberman, A. C. Rosenzweig, *Dalton Trans.* **2005**, 3390–3396.

41. A. Kitmitto, N. Myronova, P. Basu, H. Dalton, *Biochemistry* **2005**, *44*, 10954–10965.

42. N. Myronova, A. Kitmitto, R. F. Collins, A. Miyaji, H. Dalton, *Biochemistry* **2006**, *45*, 11905–11914.

43. H. J. Op den Camp, T. Islam, M. B. Stott, H. R. Harhangi, A. Hynes, S. Schouten, M. S. M. Jetten, N. K. Birkeland, A. Pol, P. F. Dunfield, *Environ. Microbiol. Rep.* **2009**, *1*, 293–306.

44. R. L. Lieberman, K. C. Kondapalli, D. B. Shrestha, A. S. Hakemian, S. M. Smith, J. Telser, J. Kuzelka, R. Gupta, A. S. Borovik, S. J. Lippard, B. M. Hoffman, A. C. Rosenzweig, T. L. Stemmler, *Inorg. Chem.* **2006**, *45*, 8372–8381.

45. A. S. Hakemian, K. C. Kondapalli, J. Telser, B. M. Hoffman, T. L. Stemmler, A. C. Rosenzweig, *Biochemistry* **2008**, *47*, 6793–6801.

46. S. I. Chan, S. S. F. Yu, *Acc. Chem. Res.* **2008**, *41*, 969–979.

47. H. H. T. Nguyen, A. K. Shiemke, S. J. Jacobs, B. J. Hales, M. E. Lidstrom, S. I. Chan, *J. Biol. Chem.* **1994**, *269*, 14995–15005.

48. H. H. T. Nguyen, K. H. Nakagawa, B. Hedman, S. J. Elliott, M. E. Lidstrom, K. O. Hodgson, S. I. Chan, *J. Am. Chem. Soc.* **1996**, *118*, 12766–12776.

49. A. C. Rosenzweig, M. H. Sazinsky, *Curr. Opin. Struc. Biol.* **2006**, *16*, 729–735.

50. H. H. A. T. Nguyen, M. Zhu, S. J. Elliott, K. H. Nakagawa, B. Hedman, A. M. Costello, T. L. Peeples, B. Wilkinson, H. Morimoto, P. G. Williams, H. G. Floss, M. E. Lidstrom, K. O. Hodgson, S. I. Chan, *Microbial Growth on C(1) Compounds* **1996**, 150–158.

51. M. Takeguchi, K. Miyakawa, I. Okura, *J. Mol. Catal. A-Chem.* **1998**, *132*, 145–153.

52. M. Takeguchi, I. Okura, *Catal. Surv. Jpn.* **2000**, *4*, 51–63.

53. H. Yuan, M. L. P. Collins, W. E. Antholine, *J. Am. Chem. Soc.* **1997**, *119*, 5073–5074.

54. H. Yuan, M. L. P. Collins, W. E. Antholine, *Biophys. J.* **1999**, *76*, 2223–2229.

55. S. S. Lemos, M. L. P. Collins, S. S. Eaton, G. R. Eaton, W. E. Antholine, *Biophys. J.* **2000**, *79*, 1085–1094.

56. L. V. Tumanova, I. A. Tukhvatullin, D. S. Burbaev, R. I. Gvozdev, K. K. Andersson, *Russ. J. Bioinorg. Chem.* **2005**, *34*, 177–185.

57. M. Martinho, D. W. Choi, A. A. DiSpirito, W. E. Antholine, J. D. Semrau, E. Münck, *J. Am Chem. Soc.* **2007**, *129*, 15783–15785.

58. O. A. Karlsen, J. R. Lillehaug, H. B. Jensen, *Mol. Microbiol.* **2008**, *70*, 15–26.

59. S. M. Smith, R. Balasubramanian, A. C. Rosenzweig, *Meth. Enzymol.* **2011**, *495*, 195–210.

60. R. Balasubramanian, S. M. Smith, S. Rawat, L. A. Yatsunyk, T. L. Stemmler, A. C. Rosenzweig, *Nature* **2010**, *465*, 115–U131.

61. A. Miyaji, T. Kamachi, I. Okura, T. Baba, *J. Mol. Catal. B-Enzym.* **2010**, *62*, 121–121.

62. J. C. Murrell, T. J. Smith, in *Handbook of Hydrocarbon and Lipid Microbiology*, Ed K. N. Timmis, Springer, Heidelberg, Germany, 2010, Vol. 1, pp. 1045–1055.

63. A. Miyaji, T. Miyoshi, K. Motokura, T. Baba, *Biotechnol. Lett.* **2011**, *33*, 2241–2246.

64. S. J. Elliott, M. Zhu, L. Tso, H. H. T. Nguyen, J. H. K. Yip, S. I. Chan, *J. Am Chem. Soc.* **1997**, *119*, 9949–9955.

65. W. J. Song, G. Gucinski, M. H. Sazinsky, S. J. Lippard, *Proc. Natl. Acad. Sci. USA* **2011**, *108*, 14795–14800.

66. K. H. C. Chen, H. H. Wu, S. F. Ke, Y. T. Rao, C. M. Tu, Y. P. Chen, K. H. Kuei, Y. S. Chen, V. C. C. Wang, W. C. Kao, S. I. Chan, *J. Inorg. Biochem.* **2012**, *111*, 10–17.

67. S. A. Cook, A. K. Shiemke, *Arch. Biochem. Biophys.* **2002**, *398*, 32–40.

68. M. R. Hyman, P. M. Wood, *Biochem. J.* **1985**, *227*, 719–725.

69. M. R. Hyman, D. J. Arp, *J. Biol. Chem.* **1992**, *267*, 1534–1545.

70. S. Gilch, M. Vogel, M. W. Lorenz, O. Meyer, I. Schmidt, *Microbiology* **2009**, *155*, 279–284.

71. G. M. Tonge, D. E. F. Harrison, C. J. Knowles, I. Higgins, *FEBS Lett.* **1975**, *58*, 293–299.

72. M. A. Culpepper, G. E. Cutsail, B. M. Hoffman, A. C. Rosenzweig, *J. Am Chem. Soc.* **2012**, *134*, 7640–7643.

73. E. I. Solomon, U. M. Sundaram, T. E. Machonkin, *Chem. Rev.* **1996**, *96*, 2563–2605.

74. E. I. Solomon, J. W. Ginsbach, D. E. Heppner, M. T. Kieber-Emmons, C. H. Kjaergaard, P. J. Smeets, L. Tian, J. S. Woertink, *Faraday Discuss.* **2011**, *148*, 11–39.

75. C. R. Andrew, K. P. McKillop, A. G. Sykes, *Biochim. Biophys. Acta* **1993**, *1163*, 17–25.

76. T. Zalateva, L. Santagostini, L. Bubacco, L. Casella, B. Salvato, M. Beltramini, *J. Inorg. Biochem.* **1998**, *72*, 211–215.

77. Y. Shiota, K. Yoshizawa, *Inorg. Chem.* **2009**, *48*, 838–845.

78. K. Yoshizawa, Y. Shiota, *J. Am. Chem. Soc.* **2006**, *128*, 9873–9881.

79. P. P. Y. Chen, S. I. Chan, *J. Inorg. Biochem.* **2006**, *100*, 801–809.

80. R. A. Himes, K. D. Karlin, *Curr. Opin. Chem. Biol.* **2009**, *13*, 119–131.

81. M. H. Groothaert, P. J. Smeets, B. F. Sels, P. A. Jacombs, R. A. Schoonheydt, *J. Am. Chem. Soc.* **2005**, *127*, 1394–1395.

82. P. J. Smeets, R. G. Hadt, J. S. Woertink, P. Vanelderen, R. A. Schoonheydt, B. F. Sels, E. I. Solomon, *J. Am. Chem. Soc.* **2010**, *132*, 14736–14738.

83. J. S. Woertink, P. J. Smeets, M. H. Groothaert, M. A. Vance, B. F. Sels, R. A. Schoonheydt, E. I. Solomon, *Proc. Natl. Acad. Sci. USA* **2009**, *106*, 18908–18913.

84. P. Vanelderen, R. G. Hadt, P. J. Smeets, E. I. Solomon, R. A. Schoonheydt, B. F. Sels, *J. Catal.* **2011**, *284*, 157–164.

85. B. Wilkinson, M. Zhu, N. D. Priestley, H. H. T. Nguyen, H. Morimoto, P. G. Williams, S. I. Chan, H. G. Floss, *J. Am. Chem. Soc.* **1996**, *118*, 921–922.

86. S. S. F. Yu, L. Y. Wu, K. H. C. Chen, W. I. Luo, D. S. Huang, S. I. Chan, *J. Biol. Chem.* **2003**, *278*, 40658–40669.

87. R. Csaki, L. Bodrossy, J. Klem, J. C. Murrell, K. L. Kovacs, *Microbiology* **2003**, *149*, 1785–1795.

88. T. Nakamura, T. Hoaki, S. Hanada, A. Maruyama, Y. Kamagata, H. Fuse, *FEMS Microbiol. Lett.* **2007**, *277*, 157–164.

89. G. P. Stafford, J. Scanlan, I. R. McDonald, J. C. Murrell, *Microbiology* **2003**, *149*, 1771–1784.

90. A. R. Theisen, M. H. Ali, S. Radajewski, M. G. Dumont, P. F. Dunfield, I. R. McDonald, S. N. Dedysh, C. B. Miguez, J. C. Murrell, *Mol. Microbiol.* **2005**, *58*, 682–692.

91. M. Merkx, S. J. Lippard, *J. Biol. Chem.* **2002**, *277*, 5858–5865.

92. M. H. Sazinsky, M. Merkx, E. Cadieux, S. Y. Tang, S. J. Lippard, *Biochemistry* **2004**, *43*, 16263–16276.

93. V. Izzo, G. Leo, R. Scognamiglio, L. Troncone, L. Birolo, A. Di Donato, *Arch. Biochem. Biophys.* **2011**, *505*, 48–59.

94. U. E. Ukaegbu, S. Henery, A. C. Rosenzweig, *Biochemistry* **2006**, *45*, 10191–10198.

95. U. E. Ukaegbu, A. C. Rosenzweig, *Biochemistry* **2009**, *48*, 2207–2215.

96. J. Scanlan, M. G. Dumont, J. C. Murrell, *FEMS Microbiol. Lett.* **2009**, *301*, 181–187.

97. V. Cafaro, V. Izzo, R. Scognamiglio, E. Notomista, P. Capasso, A. Casbarra, P. Pucci, A. Di Donato, *Appl. Environ. Microbiol.* **2004**, *70*, 2211–2219.

98. J. D. Pikus, J. M. Studts, C. Achim, K. E. Kauffmann, E. Münck, R. J. Steffan, K. McClay, B. G. Fox, *Biochemistry* **1996**, *35*, 9106–9119.

99. V. Cafaro, R. Scognamiglio, A. Viggiani, V. Izzo, I. Passaro, E. Notomista, F. D. Piaz, A. Amoresano, A. Casbarra, P. Pucci, A. Di Donato, *Eur. J. Biochem.* **2002**, *269*, 5689–5699.

100. J. G. Leahy, P. J. Batchelor, S. M. Morcomb, *FEMS Microbiol. Rev.* **2003**, *27*, 449–479.

101. E. Notomista, A. Lahm, A. Di Donato, A. Tramontano, *J. Mol. Evol.* **2003**, *56*, 435–445.

102. M. H. Sazinsky, J. Bard, A. Di Donato, S. J. Lippard, *J. Biol. Chem.* **2004**, *279*, 30600–30610.

103. M. H. Sazinsky, P. W. Dunten, M. S. McCormick, A. DiDonato, S. J. Lippard, *Biochemistry* **2006**, *45*, 15392–15404.

104. L. J. Bailey, J. G. Mccoy, G. N. Phillips, B. G. Fox, *Proc. Natl. Acad. Sci. USA* **2008**, *105*, 19194–19198.

105. B. L. Dubbels, L. A. Sayavedra-Soto, D. J. Arp, *Microbiology* **2007**, *153*, 1808–1816.

106. N. Elango, R. Radhakrishnan, W. A. Froland, B. J. Wallar, C. A. Earhart, J. D. Lipscomb, D. H. Ohlendorf, *Protein Sci.* **1997**, *6*, 556–568.

107. A. C. Rosenzweig, C. A. Frederick, S. J. Lippard, P. Nordlund, *Nature* **1993**, *366*, 537–543.

108. S. J. Lee, M. S. McCormick, S. J. Lippard, U. S. Cho, *Nature* **2013**, *494*, 380–384.

109. M. H. Sazinsky, S. J. Lippard, *J. Am. Chem. Soc.* **2005**, *127*, 5814–5825.

110. D. A. Whittington, A. C. Rosenzweig, C. A. Frederick, S. J. Lippard, *Biochemistry* **2001**, *40*, 3476–3482.

111. G. T. Gassner, S. J. Lippard, *Biochemistry* **1999**, *38*, 12768–12785.

112. L. L. Chatwood, J. Müller, J. D. Gross, G. Wagner, S. J. Lippard, *Biochemistry* **2004**, *43*, 11983–11991.

113. J. Müller, A. A. Lugovskoy, G. Wagner, S. J. Lippard, *Biochemistry* **2002**, *41*, 42–51.

114. J. L. Blazyk, G. T. Gassner, S. J. Lippard, *J. Am. Chem. Soc.* **2005**, *127*, 17364–17376.

115. J. L. Blazyk, S. J. Lippard, *Biochemistry* **2002**, *41*, 15780–15794.

116. J. L. Blazyk, S. J. Lippard, *J. Biol. Chem.* **2004**, *279*, 5630–5640.

117. D. A. Kopp, G. T. Gassner, J. L. Blazyk, S. J. Lippard, *Biochemistry* **2001**, *40*, 14932–14941.

118. K. J. Walters, G. T. Gassner, S. J. Lippard, G. Wagner, *Proc. Natl. Acad. Sci. USA* **1999**, *96*, 7877–7882.

119. S.-L. Chang, B. J. Wallar, J. D. Lipscomb, K. H. Mayo, *Biochemistry* **1999**, *38*, 5799–5812.

120. B. G. Fox, Y. Liu, J. E. Dege, J. D. Lipscomb, *J. Biol. Chem.* **1991**, *266*, 540–550.

121. Y. Liu, J. C. Nesheim, S. K. Lee, J. D. Lipscomb, *J. Biol. Chem.* **1995**, *270*, 24662–24665.

122. M. H. Sazinsky, S. J. Lippard, *Accounts Chem. Res.* **2006**, *39*, 558–566.

123. K. H. Mitchell, J. M. Studts, B. G. Fox, *Biochemistry* **2002**, *41*, 3176–3188.

124. E. Cadieux, V. Vrajmasu, C. Achim, J. Powlowski, E. Münck, *Biochemistry* **2002**, *41*, 10680–10691.

125. J. Kazlauskaite, H. A. O. Hill, P. C. Wilkins, H. Dalton, *Eur. J. Biochem.* **1996**, *241*, 552–556.

126. S. Chang, B. J. Wallar, J. D. Lipcomb, J. D. Mayo, *Biochemistry* **2001**, *40*, 9539–9551.

127. H. Brandstetter, D. A. Whittington, S. J. Lippard, C. A. Frederick, *Chem. Biol.* **1999**, *6*, 441–449.

128. J. Y. Zhang, J. D. Lipscomb, *Biochemistry* **2006**, *45*, 1459–1469.

129. A. C. Rosenzweig, P. Nordlund, P. M. Takahara, C. A. Frederick, S. J. Lippard, *Chem. Biol.* **1995**, *2*, 632.

130. D. A. Whittington, S. J. Lippard, *J. Am. Chem. Soc.* **2001**, *123*, 827–838.
131. M. P. Woodland, D. S. Patil, R. Cammack, H. Dalton, *Biochim. Biophys. Acta.* **1986**, *873*, 237–242.
132. J. G. Dewitt, J. G. Bentsen, A. C. Rosenzweig, B. Hedman, J. Green, S. Pilkington, G. C. Papaefthymiou, H. Dalton, K. O. Hodgson, S. J. Lippard, *J. Am. Chem. Soc.* **1991**, *113*, 9219–9235.
133. B. G. Fox, J. D. Lipscomb, *Biochem. Biophys. Res. Comm.* **1988**, *154*, 165–170.
134. B. G. Fox, K. K. Surerus, E. Münck, J. D. Lipscomb, *J. Biol. Chem.* **1988**, *263*, 10553–10556.
135. J. G. Dewitt, A. C. Rosenzweig, A. Salifoglou, B. Hedman, S. J. Lippard, K. O. Hodgson, *Inorg. Chem.* **1995**, *34*, 2505–2515.
136. B. G. Fox, M. P. Hendrich, K. K. Surerus, K. K. Andersson, W. A. Froland, J. D. Lipscomb, E. Münck, *J. Am Chem. Soc.* **1993**, *115*, 3688–3701.
137. M. P. Hendrich, E. Münck, B. G. Fox, J. D. Lipscomb, *J. Am. Chem. Soc.* **1990**, *112*, 5861–5865.
138. B. M. Hoffman, B. E. Sturgeon, P. E. Doan, V. J. DeRose, K. E. Liu, S. J. Lippard, *J. Am. Chem. Soc.* **1994**, *116*, 6023–6024.
139. D. A. Kopp, E. A. Berg, C. E. Costello, S. J. Lippard, *J. Biol. Chem.* **2003**, *278*, 20939–20945.
140. K. E. Liu, S. J. Lippard, *J. Biol. Chem.* **1991**, *266*, 12836–12839.
141. K. E. Liu, A. M. Valentine, D. L. Wang, B. H. Huynh, D. E. Edmondson, A. Salifoglou, S. J. Lippard, *J. Am. Chem. Soc.* **1995**, *117*, 10174–10185.
142. Y. Liu, J. C. Nesheim, K. E. Paulsen, M. T. Stankovich, J. D. Lipscomb, *Biochemistry* **1997**, *36*, 5223–5233.
143. K. E. Paulsen, Y. Liu, B. G. Fox, J. D. Lipscomb, E. Münck, M. T. Stankovich, *Biochemistry* **1994**, *33*, 713–722.
144. W. Wang, S. J. Lippard, *J. Am. Chem. Soc.* **2014**, *136*, 2244–2247.
145. C. C. Page, C. C. Moser, P. L. Dutton, *Curr. Opin. Chem. Biol.* **2003**, *7*, 551–556.
146. L. Shu, Y. Lui, J. D. Lipscomb, L. J. Que, *J. Biol. Inorg. Chem.* **1996**, *1*, 297–304.
147. D. Jackson Rudd, M. H. Sazinsky, M. Merkx, S. J. Lippard, B. Hedman, K. O. Hodgson, *Inorg. Chem.* **2004**, *43*, 4579–4589.
148. R. Davydov, A. M. Valentine, S. Komar-Panicucci, B. M. Hoffman, S. J. Lippard, *Biochemistry* **1999**, *38*, 4188–4197.
149. S. C. Pulver, W. A. Froland, J. D. Lipscomb, E. I. Solomon, *J. Am. Chem. Soc.* **1997**, *119*, 387–395.
150. N. Mitic, J. K. Schwartz, B. J. Brazeau, J. D. Lipscomb, E. I. Solomon, *Biochemistry* **2008**, *47*, 8386–8397.
151. W. A. Froland, K. K. Andersson, S. K. Lee, Y. Liu, J. D. Lipscomb, *J. Biol. Chem.* **1992**, *267*, 17588–17597.
152. J. D. Pikus, J. M. Studts, K. McClay, R. J. Steffan, B. G. Fox, *Biochemistry* **1997**, *36*, 9283–9289.
153. M. S. McCormick, M. H. Sazinsky, K. L. Condon, S. J. Lippard, *J. Am. Chem. Soc.* **2006**, *128*, 15108–15110.
154. D. A. Whittington, M. H. Sazinsky, S. J. Lippard, *J. Am. Chem. Soc.* **2001**, *123*, 1794–1795.
155. A. C. Rosenzweig, H. Brandstetter, D. A. Whittington, P. Nordlund, S. J. Lippard, C. A. Frederick, *Protein Struct. Funct. Genet.* **1997**, *29*, 141–152.
156. B. J. Wallar, J. D. Lipscomb, *Biochemistry* **2001**, *40*, 2220–2233.
157. C. E. Tinberg, S. J. Lippard, *Biochemistry* **2009**, *48*, 12145–12158.
158. S. Y. Lee, J. D. Lipscomb, *Biochemistry* **1999**, *38*, 4423–4432.
159. W. J. Song, M. S. McCormick, R. K. Behan, M. H. Sazinsky, W. Jiang, J. Lin, C. Krebs, S. J. Lippard, *J. Am. Chem. Soc.* **2010**, *132*, 13582–13585.
160. J. D. Pikus, K. H. Mitchell, J. M. Studts, K. McClay, R. J. Steffan, B. G. Fox, *Biochemistry* **2000**, *39*, 791–799.
161. N. L. Elsen, L. J. Bailey, A. D. Hauser, B. G. Fox, *Biochemistry* **2009**, *48*, 3838–3846.

162. W. J. Song, R. K. Behan, S. G. Naik, B. H. Huynh, S. J. Lippard, *J. Am. Chem. Soc.* **2009**, *131*, 6074–6075.
163. S. K. Lee, J. C. Nesheim, J. D. Lipscomb, *J. Biol. Chem.* **1993**, *268*, 21569–21577.
164. S. S. Stahl, W. A. Francisco, M. Merkx, J. P. Klinman, S. J. Lippard, *J. Biol. Chem.* **2001**, *276*, 4549–4553.
165. K. E. Liu, D. Wang, B. H. Huynh, D. E. Edmondson, A. Salifoglou, S. J. Lippard, *J. Am. Chem. Soc.* **1994**, *116*, 7465–7466.
166. L. J. Shu, J. C. Nesheim, K. Kauffmann, E. Münck, J. D. Lipscomb, L. Que, *Science* **1997**, *275*, 515–518.
167. A. M. Valentine, S. S. Stahl, S. J. Lippard, *J. Am. Chem. Soc.* **1999**, *121*, 3876–3887.
168. R. Banerjee, K. K. Meier, E. Münck, J. D. Lipcomb, *Biochemistry* **2013**, *52*, 4331–4342.
169. B. J. Brazeau, J. D. Lipcomb, *Biochemistry* **2000**, *39*, 13503–13515.
170. D. Jahng, A. K. Sun, C. S. Kim, T. K. Wood, *J. Cell. Biochem.* **1995**, *59*, 44–44.
171. W. G. Han, L. Noodleman, *Inorg. Chem.* **2008**, *47*, 2975–2986.
172. A. D. Bochevarov, J. N. Li, W. J. Song, R. A. Friesner, S. J. Lippard, *J. Am. Chem. Soc.* **2011**, *133*, 7384–7397.
173. L. J. Murray, R. Garcia-Serres, S. Naik, B. H. Huynh, S. J. Lippard, *J. Am. Chem. Soc.* **2006**, *128*, 7458–7459.
174. L. J. Murray, S. J. Lippard, *Accounts Chem. Res.* **2007**, *40*, 466–474.
175. K. P. Jensen, C. B. Bell, III., M. D. Clay, E. I. Solomon, *J. Am. Chem. Soc.* **2009**, *131*, 12155–12171.
176. L. G. Beauvais, S. J. Lippard, *J. Am. Chem. Soc.* **2005**, *127*, 7370–7378.
177. C. E. Tinberg, S. J. Lippard, *Biochemistry* **2010**, *49*, 7902–7912.
178. S.-K. Lee, B. G. Fox, W. A. Froland, J. D. Lipcomb, E. Münck, *J. Am. Chem. Soc.* **1993**, *115*, 6450–6451.
179. B. F. Gherman, M. H. Baik, S. J. Lippard, R. A. Friesner, *J. Am. Chem. Soc.* **2004**, *126*, 2978–2990.
180. D. Rinalde, D. M. Phillip, S. J. Lippard, R. A. Friesner, *J. Am. Chem. Soc.* **2007**, *129*, 3135–3147.
181. G. T. Rowe, E. V. Rybak-Akimova, J. P. Caradonna, *Inorg. Chem.* **2007**, *46*, 10594–10606.
182. G. Xue, R. De Hont, E. Münck, L. Que, *Nature Chem.* **2010**, *2*, 400–405.
183. G. Q. Xue, D. Wang, R. De Hont, A. T. Fiedler, X. P. Shan, E. Münck, L. Que, *Proc. Natl. Acad. Sci. USA* **2007**, *104*, 20713–20718.
184. S. K. Smoukov, D. A. Kopp, A. M. Valentine, R. Davydov, S. J. Lippard, B. M. Hoffman, *J. Am. Chem. Soc.* **2002**, *124*, 2657–2663.
185. K. K. Andersson, T. E. Elgren, L. Que, J. D. Lipcomb, *J. Am. Chem. Soc.* **1992**, *114*, 8711–8713.
186. N. D. Priestley, H. G. Floss, W. A. Froland, J. D. Lipcomb, P. G. Williams, H. Morimoto, *J. Am. Chem. Soc.* **1992**, *114*, 7561–7562.
187. A. M. Valentine, B. Wilkinson, K. E. Liu, S. KomarPanicucci, N. D. Priestley, P. G. Williams, H. Morimoto, H. G. Floss, S. J. Lippard, *J. Am. Chem. Soc.* **1997**, *119*, 1818–1827.
188. T. J. Sears, P. M. Johnson, P. Jin, S. Oatis, *J. Chem. Phys.* **1996**, *104*, 781–792.
189. B. F. Gherman, B. D. Dunietz, D. A. Whittington, S. J. Lippard, R. A. Friesner, *J. Am. Chem. Soc.* **2001**, *123*, 3836–3837.
190. J. M. Bollinger, Jr., C. Krebs, A. Vicol, S. Chen, B. A. Ley, D. E. Edmondson, B. H. Huynh, *J. Am. Chem. Soc.* **1998**, *120*, 1094–1095.
191. P. Moënne-Loccoz, J. Baldwin, B. A. Ley, T. M. Loehr, J. M. Bollinger, Jr., *Biochemistry* **1998**, *37*, 14659–14663.
192. J. A. Broadwater, C. Achim, E. Münck, B. G. Fox, *Biochemistry* **1999**, *38*, 12197–12204.
193. J. A. Broadwater, J. Y. Ai, T. M. Loehr, J. Sanders-Loehr, B. G. Fox, *Biochemistry* **1998**, *37*, 14664–14671.
194. A. S. Pereira, W. Small, C. Krebs, P. Tavares, D. E. Edmondson, E. C. Theil, B. H. Huynh, *Biochemistry* **1998**, *37*, 9871–9876.

195. P. Moënne-Loccoz, C. Krebs, K. Herlihy, D. E. Edmondson, E. C. Theil, B. H. Huynh, T. M. Loehr, *Biochemistry* **1999**, *38*, 5290–5295.

196. V. V. Vu, J. P. Emerson, M. Martinho, Y. S. Kim, E. Münck, M. H. Park, L. J. Que, *Proc. Natl. Acad. Sci. USA* **2009**, *106*, 14814–14819.

197. K. Kim, S. J. Lippard, *J. Am. Chem. Soc.* **1996**, *118*, 4914–4915.

198. X. Zhang, H. Furutachi, S. Fujinami, S. Nagatomo, Y. Maeda, Y. Watanabe, T. Kitagawa, M. Suzuki, *J. Am. Chem. Soc.* **2005**, *127*, 826–827.

199. Y. Dong, Y. Zhang, L. Shu, E. C. Wilkinson, L. Que, Jr., K. Kauffmann, E. Münck, *J. Am. Chem. Soc.* **1997**, *119*, 12683–12684.

200. Y. Dong, H. Fujii, M. P. Hendrich, R. A. Leising, G. Pan, C. R. Randall, E. C. Wilkinson, Y. Zang, L. Que, Jr., *J. Am. Chem. Soc.* **1995**, *117*, 2778–2792.

201. Y. Dong, L. Que, Jr., K. Kauffmann, E. Münck, *J. Am. Chem. Soc.* **1995**, *117*, 11377–11378.

202. H.-F. Hsu, Y. Dong, L. Shu, V. G. Young, Jr., L. Que, Jr., *J. Am. Chem. Soc.* **1999**, *121*, 5230–5237.

203. B. D. Dunietz, M. D. Beachy, Y. Cao, D. A. Whittington, S. J. Lippard, R. A. Friesner, *J. Am. Chem. Soc.* **2000**, *122*, 2828–2839.

204. W. Wang, R. E. Iacob, R. P. Luoh, J. R. Engen, S. J. Lippard, *J. Am. Chem. Soc.* **2014**, *136*, 9754–9762.

205. C. E. Tinberg, S. J. Lippard, *Biochemistry* **2010**, *49*, 7902–7912.